JOURNAL OF GEOPHYSICAL RESEARCH, VOL. 102, NO. D25, PAGES 29,939–29,956, DECEMBER 27, 1997

Detection and parameterization of variations in solar mid- and near-ultraviolet radiation (200–400 nm)

Judith L. Lean,[1] Gary J. Rottman,[2] H. Lee Kyle,[3] Thomas N. Woods,[2]
John R. Hickey,[4] and Lawrence C. Puga[5]

Abstract. Nimbus 7 and Solar Stellar Irradiance Comparison Experiment (SOLSTICE) spacecraft measurements of solar irradiance both exhibit variability at mid (200–300 nm) and near (300–400 nm) ultraviolet (UV) wavelengths that are attributable to the Sun's 27-day solar rotation, even though instrument sensitivity drifts obscure longer-term, 11-year cycle variations. Competing influences of dark sunspots and bright faculae are the dominant causes of this rotational modulation. Parameterizations of these influences using a newly developed UV sunspot darkening index and the Mg index facular proxy replicate the rotational modulation detected in both the broadband Nimbus 7 filter data (275–360 nm and 300–410 nm) and in SOLSTICE 1-nm spectra from 200 to 400 nm. Assuming that these rotational modulation influences scale linearly over the solar cycle, long-term databases of sunspot and global facular proxies permit estimation of 11-year cycle amplitudes of the mid- and near-UV solar spectrum, unmeasured at wavelengths longward of 300 nm because of insufficient long-term repeatability (relative accuracy) of state-of-the-art solar radiometers at these wavelengths. Reconstructions of UV irradiances throughout the 11-year solar cycle indicate variabilities of 0.173 W/m^2 (1.1%) in the integrated radiation from 200 to 300 nm and 0.24 W/m^2 (0.25%) in radiation from 300 to 400 nm. These two UV bands thus contribute about 13% and 18%, respectively, to the 1.34 W/m^2 (0.1%) total (spectrally integrated) radiative output solar cycle. The parameterizations allow customization of UV irradiance time series for specific wavelength bands required as inputs to general circulation model simulations of solar cycle forcing of global climate change, and have practical implications regarding the long-term repeatability required for future solar monitoring.

1. Introduction

Energy radiates from the Sun to the Earth over the entire electromagnetic spectrum, powering the climate system and creating the ozone layer. The flux of this energy, the amplitude of its response to solar activity, and its impact on the Earth's environment depend strongly on wavelength. Reliable quantification of solar spectrum variability influences on the terrestrial environment is necessary to properly deduce the magnitude of concurrent anthropogenic influences on surface temperature and ozone concentrations [*National Research Council*, 1994].

Establishing whether apparent statistical connections between solar variability and climate change [*Labitzke and van-Loon*, 1993a, b; *Lean and Rind*, 1997] are coincidental or attributable to real solar-terrestrial processes requires sophisticated simulations of the climatic response to radiative output variations across the entire solar spectrum, over a wide range of solar activity conditions [*Haigh*, 1994, 1996; *Rind and Balachandran*, 1995]. In this regard, knowledge of the mid- and near-UV spectrum variability is important for understanding global change issues related to both ozone depletion [*Wuebbles et al.*, 1991; *Huang and Brasseur*, 1993; *Balachandran and Rind*, 1995; *Fleming et al.*, 1995; *McCormack and Hood*, 1996] and surface warming [*Pollack et al.*, 1979; J. Hansen, private communication, 1996].

The Sun emits UV radiation from 200 to 400 nm with the spectral distribution shown in the top panel of Figure 1 and a flux of 111 W/m^2, equal to 8% of its total radiative output at all wavelengths of 1367 W/m^2. A part of this UV energy is deposited in the Earth's atmosphere at altitudes shown in the bottom panel of Figure 1: solar energy at wavelengths longer than 310 nm penetrates to the biosphere, while the troposphere and stratosphere absorb radiation at 295–310 nm and 200–295 nm, respectively. Variations in the solar mid- and near-UV radiation thus have the potential to naturally change the Earth's atmosphere [*Brasseur*, 1993; *Hood et al.*, 1993; *Hood*, 1997; *Chandra and McPeters*, 1994; *Jackman et al.*, 1996], possibly impacting the Earth's surface temperature indirectly via radiative and dynamical coupling processes [*Lacis et al.*, 1990; *Rind and Balachandran*, 1995]. Furthermore, changes in the UV energy that is absorbed in the middle atmosphere contribute significantly to the variability of the Sun's total (spectrally integrated) irradiance. Simulations of Earth's surface temperature change arising from solar radiative forcing must account for this diminishment of direct solar radiative forcing by adjusting total solar irradiance variability accordingly.

Limitations of present-day solar monitoring confine obser-

[1]E. O. Hulburt Center for Space Research, Naval Research Laboratory, Washington, D. C.
[2]Laboratory for Atmospheric and Space Physics, University of Colorado, Boulder.
[3]NASA Goddard Space Flight Center, Greenbelt, Maryland.
[4]Eppley Laboratory, Inc., Newport, Rhode Island.
[5]NOAA Space Environment Laboratory, Boulder, Colorado.

Paper number 97JD02092.
0148-0227/97/97JD-02092$09.00

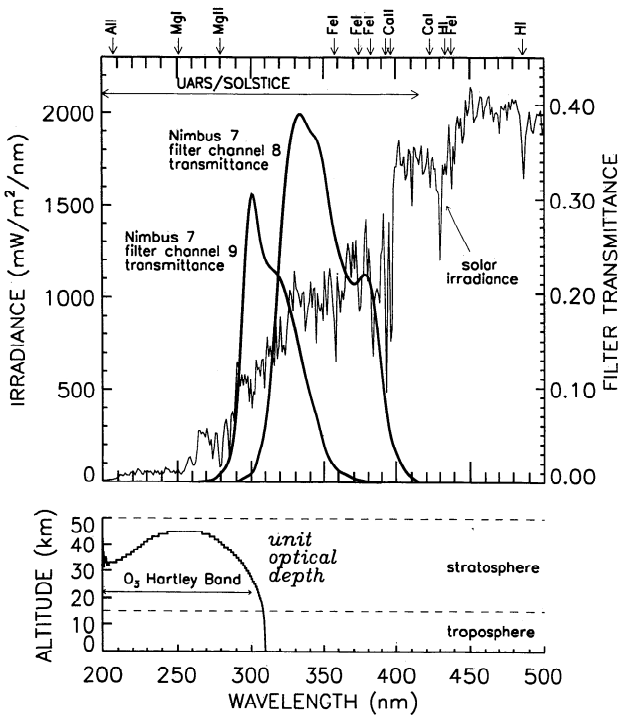

Figure 1. (top) Solar spectrum from 200 to 500 nm, measured by SOLSTICE on UARS at wavelengths less than 415 nm, and by the solar spectrometer on ATLAS at longer wavelengths (G. Thuillier, private communication, 1995). Also shown are the transmittances of Nimbus 7 filter channels 8 and 9. Wavelengths are identified for prominent spectral features attributable to various absorbing and ionizing species in the Sun's atmosphere. (bottom) Unit optical depth for the absorption of the solar spectrum in the Earth's atmosphere.

vational knowledge of the Sun's radiative output variability to the total radiation, dominated by the visible and near-infrared (IR) spectrum, and UV radiation at wavelengths shorter than about 250 nm, obtained respectively by broadband cavity radiometers [*Willson and Hudson*, 1991; *Hoyt et al.*, 1992; *Lee et al.*, 1995] and UV spectroradiometers with in-flight sensitivity tracking [*Rottman*, 1988; *Rottman et al.*, 1993; *Brueckner et al.*, 1993; *London et al.*, 1993; *Woods et al.*, 1993, 1996; *Cebula et al.*, 1996; *Thuillier et al.*, 1997]. At wavelengths longward of about 300 nm the nature and extent of variability in the solar spectrum remains poorly known, limited by inadequate long-term measurement repeatability to only a few highly uncertain estimates [*Heath*, 1980; *Hickey et al.*, 1982; *Heath and Schlesinger*, 1986; *Lean*, 1989; *Schlesinger and Cebula*, 1992; *Rottman*, 1995].

UV radiation at wavelengths from 250 to 400 nm is thought to vary over the Sun's 11-year cycle somewhat more than the 0.1% change in total radiation but less than the percentage changes that occur at shorter UV wavelengths [*Schlesinger and Heath*, 1988; *Lean*, 1991]. Analysis and interpretation of variations at both longer (total) and shorter UV wavelengths suggests that solar activity also modulates the 200- to 400-nm solar radiation through the competing influences of sunspots and faculae (in both compact active regions and extended active network) [*Foukal and Lean*, 1988; *Livingston et al.*, 1988; *Willson and Hudson*, 1991; *Lean et al.*, 1992; *Cebula et al.*, 1992; *DeLand and Cebula*, 1993; *Fröhlich*, 1994], with the role of sunspots increasing relative to faculae towards longer wavelengths [*Lean*, 1991]. Figure 2 illustrates the continuous variations in bolometric (i.e., spectrally integrated) radiation from sunspots and faculae throughout the 11-year cycle in response to variable magnetic flux within the Sun's atmosphere. Whereas sunspot influences on total radiative output dominate the shorter-term timescales of the Sun's 27-day rotation, faculae (associated with both active region plages and bright extended chromospheric network) control the 11-year total irradiance cycle. In contrast, at UV wavelengths below 200 nm, variations in faculae (i.e., plage and network) alone account for much of the observed variability over both the rotational and 11-year cycles [*Lean*, 1987; *White et al.*, 1990; *Chandra et al.*, 1995].

Although both broadband and spectrally dispersing UV radiometers have monitored the disk-integrated solar radiation in the region 200–400 nm during the past few decades [*Hickey et al.*, 1982; *Schlesinger and Heath*, 1988; *Rottman*, 1988; *Kyle et al.*, 1993; *Woods et al.*, 1996], significant instrumental effects preclude determination of real solar variability directly from the data at wavelengths longer than about 250 nm. Sensitivity drifts associated with inconstant instrument temperature and the aspect angle of the monitor relative to the Sun, and with exposure to solar radiation, limit long-term measurement repeatability to, at best, the ±1% relative accuracy goal of present state-of-the-art solar UV monitors [*Rottman et al.*, 1993; *Brueckner et al.*, 1993; *Woods et al.*, 1993, 1996]. Analyses of UV irradiance data for episodes of pronounced rotational modulation indicate that the near-UV solar spectrum varies by a few tenths of a percent [*Hickey et al.*, 1982; *London et al.*, 1993; *DeLand and Cebula*, 1993; *Rottman*, 1995], which is a factor of 5–10 smaller than the long-term repeatability of the

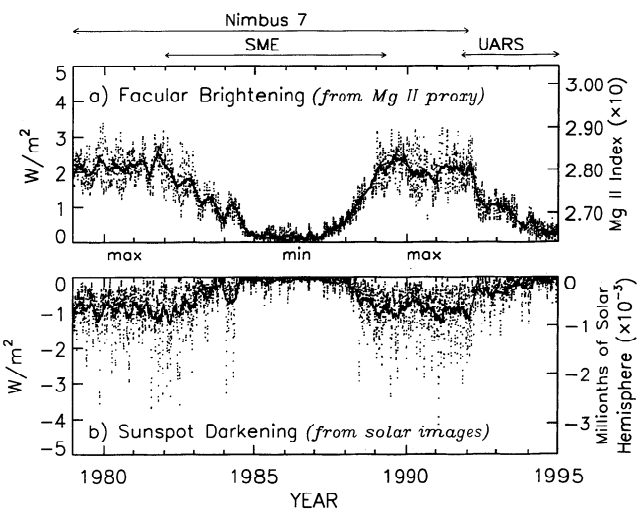

Figure 2. Continuous alteration of (a) facular brightening and (b) sunspot darkening by solar activity over both the shorter 27-day timescale of the Sun's rotation and the much longer 11-year cycle. Dots denote the daily bolometric energy variations associated with sunspot and facular modulation of the Sun's total radiative output at the energy levels shown on the left ordinates. The solid lines indicate 81-day running means of the daily data. The facular brightening is determined from the Mg II index, and sunspot darkening is determined from visible solar images using data archived at the NOAA World Data Center. The units of these proxies are shown on the right ordinates. Identified along the top of the figure are the epochs of irradiance observations by solar monitors on Nimbus 7, SME, and UARS.

solar monitoring instruments. Scalings of the rotational modulation measured by the Solar Backscatter Ultraviolet (SBUV) instrument on Nimbus 7 with a facular proxy suggest solar cycle amplitudes of 0.85% for radiation in the wavelength band 200–300 nm, and 0.09% for 300- to 400-nm radiation [*Lean*, 1989]. Spectral irradiance changes in 1-nm bands may be negligible at some near UV wavelengths and as much as 1% in the cores of Fraunhofer lines [*DeLand and Cebula*, 1993].

This paper utilizes a newly developed index of UV sunspot darkening together with the Mg index facular proxy to detect solar-related variations in spacecraft observations of the mid- and near-UV solar radiation, the latter being a region of the Sun's spectrum whose variations are poorly known. Following the removal of long-term trends to eliminate instrumental drifts, multifunctional fittings of the irradiance time series with similarly detrended sunspot and facular proxies provide numerical parameterizations of these influences, and their wavelength dependencies. Assuming that the relationships among the proxies and the irradiance evident during solar rotational modulation persists over the solar cycle, long term sunspot and facular proxy records then permit the reconstruction of the 11-year cycle modulation of mid- and near-UV solar radiation, which insufficient measurement repeatability precludes by direct observation at wavelengths longer than 300 nm.

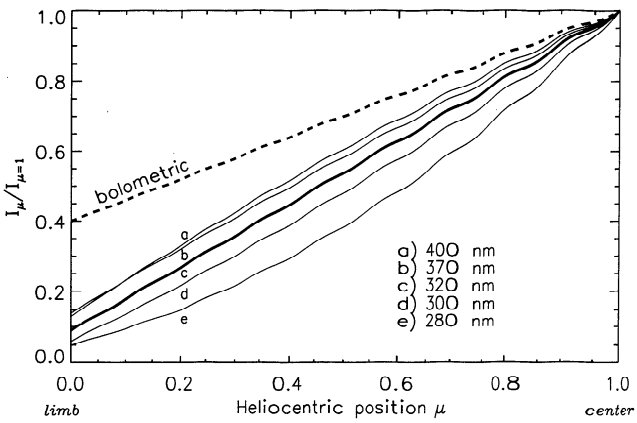

Figure 3. Variations in the emission of radiation from a specified radial location on the Sun's disk relative to that at disk center for bolometric and UV radiation at wavelengths from 280 to 400 nm (identified as lines a–e) from *Allen* [1981]. The thickest solid line (line c) corresponds to the limb variation at 320 nm, which is used to numerically calculate UV sunspot darkening.

2. Proxies for Sunspot Darkening and Facular Brightening

On any given day, both sunspots and faculae (accompanied by their chromospheric counterparts, plages) are usually present on the Sun's disk. Depending on their areas, locations and brightnesses relative to the background Sun, these features alter the otherwise homogeneous distribution of the disk emission, causing a net energy change in radiative output. During solar minimum conditions sunspots and faculae may be absent entirely from the Sun's disk for days at a time, whereas their presence is commonplace at activity maximum. A variety of spatially resolved and global solar observations made from the ground and space provide data with which to construct proxy representations of sunspot and faculae influences on global solar radiative output, independently of the directly measured irradiances. We develop formulations appropriate for sunspot darkening and facular brightening in the wavelength range 200–400 nm in this section and utilize these formulations in section 4 to parameterize UV irradiance variability.

2.1. UV Sunspot Darkening

Foukal [1981] and *Fröhlich et al.* [1994] estimate the change in radiation, $\Delta F(\lambda)_S$, at wavelength λ, attributable to a sunspot of area A relative to the background disk-integrated radiation $F(\lambda)$, as

$$\frac{\Delta F(\lambda)_S}{F(\lambda)} = \frac{5\mu A_{\mathrm{WDC}}[C_S(\lambda) - 1]R(\lambda, \mu)}{2} \qquad (1)$$

where $A_{\mathrm{WDC}} = A/(2\pi R_{\mathrm{SUN}}^2)$ (provided in units of millionths of the solar hemisphere by the National Oceanic and Atmospheric Administration World Data Center) is the fraction of the visible spherical hemisphere covered by the sunspot for solar radius R_{SUN} and the sunspot's heliocentric location is μ (cosine of position angle with respect to solar disk center). The contrast of the sunspot, $C_S(\lambda) = I_S(\lambda)/I(\lambda)$, is the ratio of the mean specific intensity of the spot, $I_S(\lambda)$, relative to that of the background solar photosphere, $I(\lambda)$. Equation (1) assumes that $C_S(\lambda)$ is the same for sunspots at different positions on the solar disk (i.e., invariant with respect to μ [*Allen*, 1981]). $R(\lambda, \mu) = I(\lambda, \mu)/I_0(\lambda)$ is the center-to-limb variation of photospheric specific intensity $I(\lambda, \mu)$ at heliocentric position μ relative to that at the center of the disk, $I_0(\lambda)$.

For bolometric (i.e., spectrally integrated) radiation $R^{\mathrm{BOL}}(\mu) = (3\mu + 2)/5$ [*Foukal*, 1981] and denoting $S = \int F(\lambda)\, d\lambda$, equation (1) reduces to

$$\frac{\Delta S_S}{S} = \frac{\mu(3\mu + 2)A_{\mathrm{WDC}}(C_S^{\mathrm{BOL}} - 1)}{2} \qquad (2)$$

Summing (2) over all sunspots present on the disk yields the so-called bolometric sunspot blocking function P_S^{BOL} [*Foukal*, 1981], also called the photometric sunspot index [*Willson and Hudson*, 1991; *Chapman et al.*, 1989; *Fröhlich*, 1994], where $C_S^{\mathrm{BOL}} - 1 = -0.3235$ [*Allen*, 1981]. Recent studies provide empirical evidence for the dependence of sunspot contrast on sunspot area, in the sense that larger sunspots are darker than smaller sunspots. According to *Brandt et al.* [1994],

$$C_S^{\mathrm{BOL}} - 1 = -[0.2231 + 0.0244 \log_{10}(A_{\mathrm{WDC}})] \qquad (3)$$

Figure 2b shows bolometric energy changes attributable to the net sunspot blocking from 1979 to 1995, obtained by summing (2) and (3) over all sunspots on the disk, with $S = 1367$ W/m^2.

At UV wavelengths, both the sunspot contrasts and the center-to-limb variations differ from their bolometric counterparts. Figure 3 compares the bolometric quantity $(3\mu + 5)/2$ with UV center-to-limb functions given by $R(\lambda, \mu) = 1 - u(\lambda) - v(\lambda) + u(\lambda)\mu + v(\lambda)\mu^2$, where u and v are numerical quantities that *Allen* [1981] provides for wavelength-dependent determination of $R(\lambda, \mu)$. *Allen* [1981] also provides numerical values for sunspot contrasts, denoted here as $C_S^{\mathrm{ALLEN}}(\lambda)$ and shown in Figure 4. Lacking specific measurements of the area dependence of sunspot contrasts at UV wavelengths, but assuming that the bolometric area dependence also applies to UV radiation, then

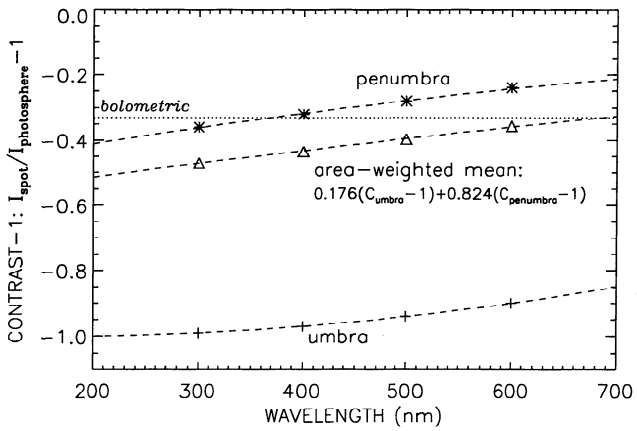

Figure 4. Spot umbral (crosses) and penumbral (asterisks) emissions ratioed to the background photosphere, from *Allen* [1981]. Sunspots are dark relative to radiation from the background photosphere, with emission from the central umbra reduced below that from the surrounding penumbra. Values of the area-weighted mean residual contrasts of sunspots at different wavelengths (triangles) are used to calculate sunspot darkening for the mid- and near-UV spectrum. For comparison, the bolometric sunspot contrast is also shown (dotted lines).

$$C_S(\lambda) - 1 = \frac{[C_S^{\mathrm{ALLEN}}(\lambda) - 1]}{0.3235} \cdot [0.2231 + 0.0244 \log_{10}(A_{\mathrm{WDC}})] \quad (4)$$

where the ratio $[C_S^{\mathrm{ALLEN}}(\lambda) - 1]/0.3235$ simply renormalizes the sunspot contrast from bolometric to UV levels. Figure 5 compares bolometric and UV sunspot darkening at 320 nm where, as in Figure 2, P_S^{BOL} is determined by summing (2) and (3) over all spots on the disk, while P_S^{320} is determined analogously by evaluating equations (1) and (4) at 320 nm with $R(\mu) = 0.09 + 0.88\mu + 0.03\mu^2$ and $C_S - 1 = -0.464/0.3235[0.2231 + 0.0244 \log_{10}(A_{\mathrm{WDC}})]$. The bolometric and UV sunspot darkening functions are highly correlated, having correlation coefficients greater than 0.99 for all years. This suggests that the differences in Figure 3 between the bolometric and UV center-to-limb functions have minimal impact on the temporal structure of sunspot blocking. Rather, the wavelength-dependent sunspot contrast (Figure 4) is the primary cause of differences in Figure 5 between the bolometric and UV sunspot blocking. Neglecting even smaller differences seen in Figure 3 among the UV center-to-limb functions, the subsequent analysis utilizes P_S^{320} in lieu of evaluating the sunspot blocking with wavelength-dependent center-to-limb functions. Thus, from (1) and (4),

$$P_S^{\mathrm{UV}}(\lambda, t) = \sum \frac{5\mu(t)A_{\mathrm{WDC}}(t)}{2} \times \frac{[C_S^{\mathrm{ALLEN}}(\lambda) - 1]}{0.3235} \cdot [0.2231 + 0.0244 \log_{10}(A_{\mathrm{WDC}}(t))] \cdot [0.09 + 0.88\mu(t) + 0.03\mu(t)^2] = \frac{[C_S^{\mathrm{ALLEN}}(\lambda) - 1]}{0.464} \times P_S^{320}(t) \quad (5)$$

2.2. UV Facular Brightening

In principle, an approach analogous to equation (1) can estimate the change in radiation, $\Delta F(\lambda)_F$, attributable to faculae on the solar disk [*Foukal*, 1981]. However, the uncertainties are much larger because observational determination of facular areas and contrast are significantly less reliable than for sunspots. Compared with the compact sunspots, faculae are more dispersed on the solar disk and have much lower bolometric contrasts (a few versus 30%). Some studies have developed facular brightening functions for prominent active regions using Ca K solar images to identify these features by their much brighter chromospheric surrogates, plages [*Vrsnak et al.*, 1991; *Steinegger et al.*, 1996]. Magnetic activity also produces smaller faculae within the network of enhanced emission that covers the entire solar disk; these smaller faculae are indistinguishable from the network that composes the background "quiet" photosphere [*Harvey and White*, 1996; *Foukal*, 1996]. It has proven extremely difficult to quantify properly the contribution of "active network" faculae to irradiance modulation [*Foukal et al.*, 1991; *Nishikawa*, 1991; *Lawrence et al.*, 1991]. As a result, the direct specification of the global, disk-integrated facular signal has yet to be adequately implemented into the determination of solar radiative output changes.

Lacking direct determination of P_F^{UV} from solar imagery, certain full-disk indices can serve as proxies, denoted P_F^{PROX}, for the facular brightness component of solar irradiance variability. Previous studies at both longer (total) and shorter UV wavelengths support the use of the Ca II and Mg II indices and the equivalent width (EW) of the He I 1083-nm line [*Harvey and Livingston*, 1994]. The Ca and Mg indices are determined as ratios of emission in the cores of these Fraunhofer lines to that in the nearby continuum and hence are also known as core-to-wing ratios [*White and Livingston*, 1981; *Donnelly*, 1988a; *White et al.*, 1990; *DeLand and Cebula*, 1993; *deToma et al.*, 1997]. After removing the sunspot darkening P_S^{BOL} from measured total solar irradiance S, the residuals $S_{\mathrm{RES}} = S(1 - P_S^{\mathrm{BOL}})$ closely track the He EW, Ca II, and Mg II indices [*Foukal and Lean*, 1988; *Livingston et al.*, 1988]. Linear regression then yields a conversion from the facular proxy to energy units of the total irradiance brightening component. The facular brightening variations shown in Figure 2 were deduced in this way using the measurements of S made by the Active Cavity

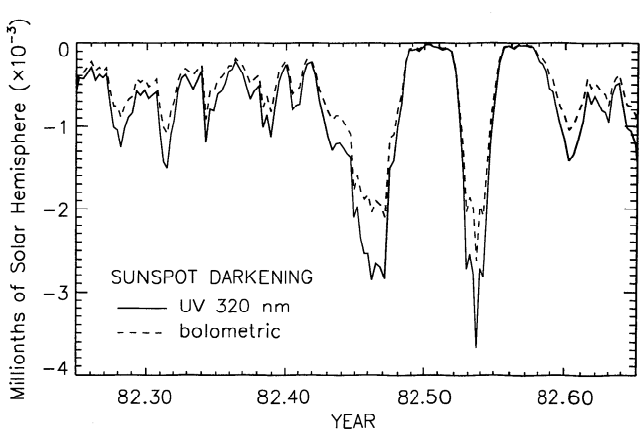

Figure 5. Comparison of sunspot blocking calculations for bolometric and UV radiation at 320 nm during 1982. The overall sunspot darkening is greater at UV wavelengths (solid line) than for bolometric radiation (dashed lines) because sunspot contrast is somewhat larger, as is shown in Figure 4. On the scale of this figure, differences attributable to the different UV center-to-limb variations shown in Figure 3 are negligible.

Radiometer Irradiance Monitor (ACRIM I) on the Solar Maximum Mission (SMM) spacecraft from 1980 to 1989, and the Mg II index for P_F^{PROX} over the same time period.

Independent studies indicate that UV irradiance rotational modulation at wavelengths shortward of 200 nm, where sunspot effects are minimal, also correlate well with both the Mg index and He EW facular proxies [*Donnelly*, 1988b; *White et al.*, 1990; *Chandra et al.*, 1995], although underpredicting somewhat the variance near 13 days relative to that at 27 days in the mid-UV spectrum [*Donnelly and Puga*, 1990]. Recent analysis of the short- and long-term irradiance changes measured by solar UV monitoring instruments on the Upper Atmosphere Research Satellite (UARS) suggests that the scaling of rotational and solar cycle modulation is equivalent for most of the far-UV spectrum at wavelengths from 130 to 200 nm [*Chandra et al.*, 1995]. However, the UARS data also indicate that this simple assumption of equivalence of rotational and cyclic proxy scalings may not be valid for the Lyman α irradiance at 121 nm [*Chandra et al.*, 1995; *Woods and Rottman*, 1997], and questions exist about its validity for certain other emission lines in the far-UV spectrum. Despite some limitations of their applicability for solar irradiance variability, especially over shorter timescales, the Mg II core-to-wing index and the He I EW remain the most suitable global facular proxies for analysis to deduce longer-timescale variations. Chosen for our subsequent analysis of the mid- and near-UV solar spectrum from 200 to 400 nm is the Mg II core-to-wing index produced by the NOAA Space Environment Laboratory. Using the He EW yields essentially equivalent results.

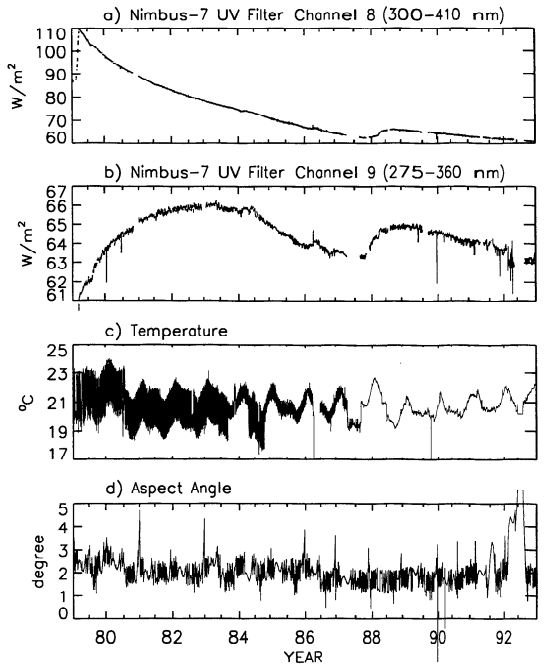

Figure 6. Signals recorded by (a) filter channel 8 and (b) filter channel 9 of the ERB experiment on board the Nimbus 7 spacecraft, and (c) the temperature and (d) the aspect angle of the ERB instrument during flight. The filter channel signals are converted to units of irradiance (W/m^2) on the basis of prelaunch calibrations.

3. Detection of Mid- and Near-UV Irradiance Variations

3.1. Nimbus 7 ERB UV Filter Channels

From November 1978 until the end of 1992, filter thermopile detectors onboard the Nimbus 7 spacecraft monitored the Sun's UV radiation in two broad bands: 275–360 nm and 300–410 nm. Figure 1 shows the passbands of the two Nimbus 7 UV filters determined prior to launch and denoted filter channels 9 and 8, respectively, of the Earth Radiation Budget (ERB) instrument [*Hickey et al.*, 1982; *Kyle et al.*, 1993]. Tests of spare Nimbus 7 ERB components flown on the Long Duration Exposure Facility (LDEF) indicate that small wavelength-dependent changes may occur in the effective filter passbands in orbit [*Hickey*, 1991] but quantitative information is unavailable for the flight filters.

Evidence for real solar variations is not readily apparent in the raw data from the UV channels, shown in their entirety in Figure 6a and 6b, along with their changing thermal and aspect environments (Figure 6c and 6d), and with greater clarity in Figure 7 during 1982 and 1990. Significant trends in the filter radiometer signals (of the order of 5% in channel 9 and 50% in channel 8) are evident over timescales of years and are associated primarily with the modification by high-energy solar radiation and atomic oxygen of the transmissivity of the radiometers' outer Suprasil W windows [*Predmore et al.*, 1982; *Hickey*, 1991]. That the spectral filter of channel 8 contained lead, whereas that of channel 9 did not, may explain their significantly different long-term degradations; the development of pinholes in the filters is also speculated as a cause of these differences [*Kyle et al.*, 1993]. Temperature drifts cause primarily day-to-day changes, and field-of-view drifts have effects on timescales of weeks. Temperature and field-of-view fluctuations both affect the raw filter signals at levels of a few tenths of a percent. These instrumental changes are comparable to the changes expected from the Sun's 27-day rotation and, for detection of real solar variability, must be removed from the raw data.

Day-to-day temperature fluctuations from 19° to 22°C (e.g., Figure 7c) affect the Nimbus 7 measurements. Scatterplots in Figure 8a and 8c of filter channel 9 and 8 signals and their temperatures, following subtraction of 3-day running means, indicate signal temperature sensitivities of 0.05 W/m^2 per 2°C (equivalent to 0.08% of the signal) for channel 9 and -0.027 W/m^2 per 2°C for channel 8. Linear regressions of the data in Figure 8 permit normalization of the filter channel signals to a mean temperature of 20.75°C.

Aspect angle changes occur over timescales of weeks and months, somewhat longer than the day-to-day temperature fluctuations, and also alter the Nimbus 7 filter channel signals. These effects are evaluated after the temperature normalization. Figures 8b and 8d are scatterplots of the temperature-corrected signals versus aspect following subtraction of 11-day running means from both. Linear relationships determined from the data allow removal of aspect effects from the filter channel signals, normalizing to the mean aspect angle of 2°. Note that channel 9 is significantly more sensitive to aspect (0.2 W/m^2, or 0.15% of the signal, per 1° of aspect) than is channel 8 (-0.005 W/m^2 per 1° of aspect), and this is evident in the larger short-term fluctuations of the raw data in Figure 6. This difference in aspect sensitivity of the two channels is likely attributable to differences in the cosine response of their respective filters.

Long-term sensitivity drifts of the order of a few percent in

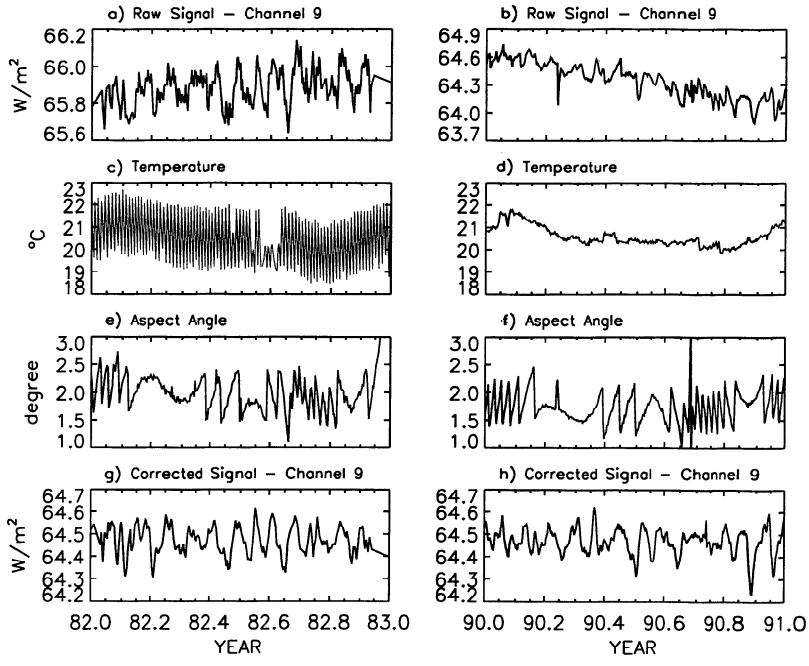

Figure 7. Raw Nimbus 7 filter channel 9 signals during (a) 1982 and (b) 1990, taken from the data in Figure 6, with (c, d) corresponding temperature changes and (e, f) the aspect variations, also from Figure 6, and (g, h) residual variations following correction of the raw signals for temperature and aspect sensitivities and removal of overall long-term sensitivity drifts.

channel 9 and factors of 2 in channel 8 dominate the Nimbus 7 filter channel signals after correction for instrument temperature and aspect. Subtracting 35-day running mean values detrends the UV filter channel signals, revealing the residual variations shown in Figures 7g and 7h. Since this detrending removes long-term trends attributable to either or both instrumental sensitivity and solar activity, the corrected signals reflect only the influences of short- and intermediate-term solar variability, arising from predominantly rotational modulation, that are in reality superimposed on longer-term solar cycle changes.

Figure 9 illustrates that following adjustment for their respective temperature, aspect, and long-term sensitivity changes, the corrected Nimbus 7 filter channel 8 and 9 signals

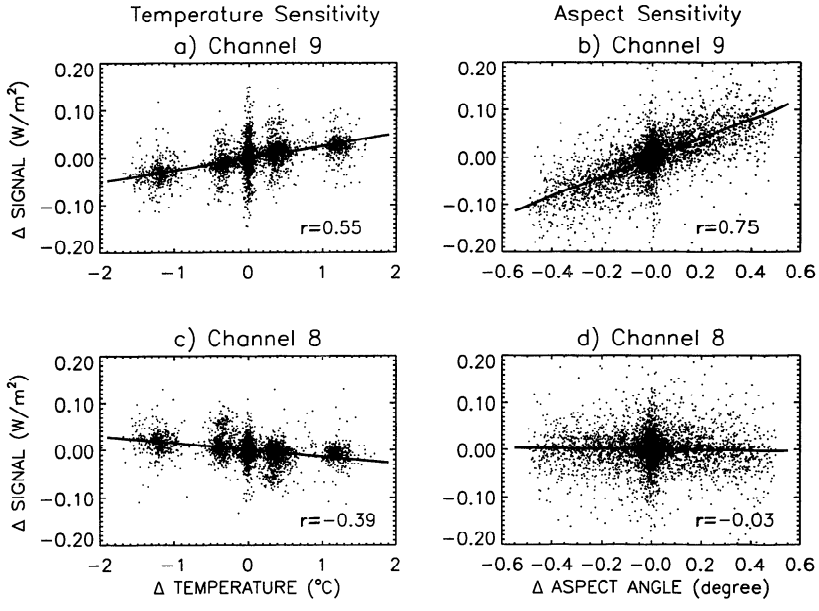

Figure 8. Linear relationships of the Nimbus 7 filter channels with temperature and aspect, accomplished with scatterplots of signal and temperature differences relative to 3-day running means, for channel 9 (Figure 8a) and for channel 8 (Figure 8c). Following the application of the temperature corrections, scatterplots of the signal and aspect differences relative to 11-day means provide the aspect calibration for channel 9 (Figure 8b) and channel 8 (Figure 8d).

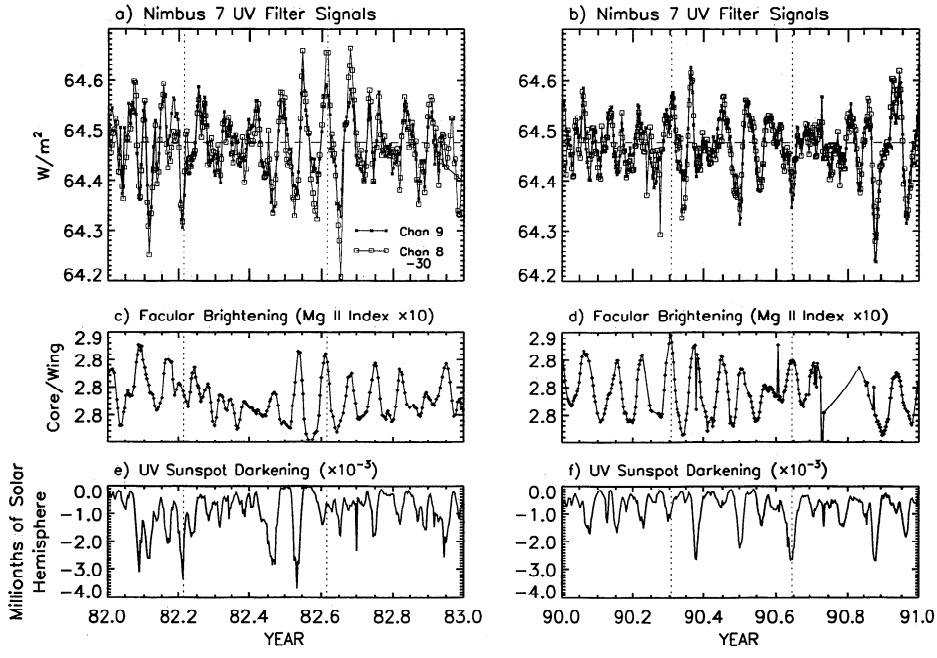

Figure 9. Comparison of corrected Nimbus 7 filter channel signals with sunspot and facular proxies. After correction for temperature, aspect, and long-term sensitivity drifts, the channel 8 (open squares) and channel 9 (asterisks) signals indicate very similar variations, as evidenced by their data during (a) 1982 and (b) 1990. Comparisons of the simultaneous variations recorded by both filter radiometers (after correction for temperature, aspect and trends) with (c, d) facular brightening and (e, f) sunspot darkening demonstrate clear evidence for the presence of real solar variability in the filter radiometer data. The long-dashed horizontal lines in Figures 9a and 9b indicate the mean level of the corrected signal relative to which the short-term variations are shown. The short-dashed vertical lines identify episodes of sunspot darkening and facular brightening to demonstrate the concurrent signal changes of the order of a few tenths of a percent relative to the mean signal level associated with these solar effects.

track each other very closely, with correlation coefficients of 0.85 in both 1982 and 1990 (i.e., the data in Figures 9a and 9d). This close agreement of the variability evident in the two corrected UV filter channel signals is achieved only after removing aspect, temperature and long-term drifts of quite different magnitudes (Figure 8).

Comparison in Figure 9 of the corrected filter channel signals with sunspot and facular proxies supports the contention that these data exhibit real solar variability. The four thin dashed lines in Figure 9 identify specific examples of such episodes. Prominent facular brightening in June–July 1982 (at 82.6 in Figure 9) is associated with an increase of about 0.13 W/m^2 (or 0.2%) in the channel 9 corrected signal relative to its mean value of 64.47 W/m^2. In contrast, during March 1982 (82.2 in Figure 9) a decrease of 0.15 W/m^2 (0.3%) occurs at a time of pronounced sunspot darkening. Likewise, signal modulations of $\pm$0.1 to 0.2 W/m^2 occur in 1990 associated with facular enhancement (e.g., at 90.31) and sunspot darkening (e.g., at 90.65).

3.2. UARS SOLSTICE

Launched in September 1991 on board UARS, the Solar-Stellar Irradiance Comparison Experiment (SOLSTICE) is presently monitoring solar UV spectral radiation at wavelengths from 115 to 415 nm [*Rottman et al.*, 1993; *London et al.*, 1993; *Woods et al.*, 1993]. While the SOLSTICE raw signals are sensitive to a myriad of environmental influences including instrument solar pointing and spacecraft temperature, extensive preflight and in-flight radiometric characterizations enable detailed evaluation of these effects and their removal from the data. Regular observations of an ensemble of bright UV stars provide in-flight, end-to-end tracking of SOLSTICE's radiometric sensitivity with a long-term repeatability goal of $\pm$1%. The SOLSTICE spectra archived on a 1-nm grid in the Goddard Space Flight Center Distributed Active Archive Center (DAAC) (data version 8) have all presently known instrumental effects removed (although work continues to further refine the data) [*Woods et al.*, 1996]. In these data, day-to-day (i.e., shorter term) repeatability approaches at times the level of a few tenths of a percent typical of the UV irradiance variations detected in the Nimbus 7 filter channel data (Figure 9).

Nevertheless, examples of SOLSTICE signal variations at selected UV wavelengths shown in Figure 10 indicate that signal drifts probably obscure real solar variability at the longest UV wavelengths, other than during a few selected episodes of large sunspot influence [*Rottman*, 1995]. The SOLSTICE data can provide only an upper limit of about $\pm$1% for the variability of solar radiation at wavelengths longer than 300 nm. For this reason, in the following analyses, long-term trends are removed from the SOLSTICE data, as per the Nimbus 7 data, in order to isolate real short- and intermediate-term solar variations from long-term changes, whether arising from solar variability or changes in instrumental sensitivity.

Linear correlation coefficients in Figure 11 of SOLSTICE daily spectra in 1-nm bins with the Mg II index facular proxy (after detrending both data sets by removing 35-day running means) are high (~0.85) for wavelengths near 200 nm, reflect-

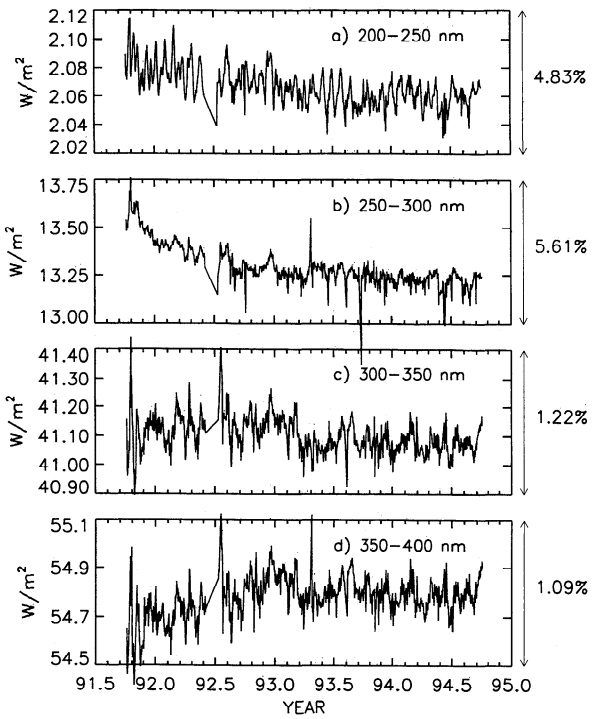

Figure 10. Shown are records of UV radiation from late 1991 to mid 1994 (years of generally decreasing solar activity, as indicated in Figure 2) determined by summing the measured SOLSTICE version 8 daily 1-nm spectra into 50-nm bins from (a) 200 to 250 nm, (b) 250 to 300 nm, (c) 300 to 350 nm, and (d) 350 to 400 nm.

ing predominantly facular/plage modulation of this radiation. However, the facular proxy alone explains little of the variance in the near UV spectrum from 300 to 400 nm, where correlation coefficients are typically in the range ±0.1. In contrast, the multiple correlation coefficient between the SOLSTICE daily spectra and facular and sunspot proxies together is notably larger in the wavelength region from 300 to 400 nm, suggesting the presence of real sunspot-related solar variability in the SOLSTICE data, albeit at approximately the noise level.

4. Parameterizations of UV Irradiance Variability Using Sunspot and Facular Proxies

The detection of solar variability signatures in both the Nimbus 7 and SOLSTICE data associated with sunspot darkening and facular brightening suggests that parameterizations can be developed to quantify the variability amplitudes in response to solar activity and thus to numerically reconstruct mid- and near-UV spectrum variations over longer timescales using the proxy data. With this goal, two separate approaches are employed. First, the Nimbus 7 and SOLSTICE UV irradiance data are modeled statistically with a combination of sunspot darkening and facular brightening proxy functions, using multiple linear regression to establish their relative amplitudes at different wavelengths. An alternate approach removes the calculated UV sunspot blocking from the irradiance data at each wavelength and then correlates the residuals with the Mg index facular proxy. This second approach mimics the technique employed in studies of total irradiance variations [*Foukal and Lean*, 1988].

4.1. Multiple Regression Analysis

A time series $F(\lambda, t)$ of UV irradiance at wavelength λ, whose modulations are assumed to arise from sunspot darkening proportional to $P_S^{320}(t)$ (equation (5)), and facular brightening, represented by $P_F^{\mathrm{PROX}}(t)$ (taken as the Mg II index), is modeled according to

$$F(\lambda, t) = a(\lambda) + b(\lambda)P_F^{\mathrm{PROX}}(t) + c(\lambda)P_S^{320}(t) \qquad (6)$$

using multiple linear least squares regression to determine the coefficients $a(\lambda)$, $b(\lambda)$, and $c(\lambda)$.

In the case of each Nimbus 7 filter channel, $F(\lambda, t)$ is the

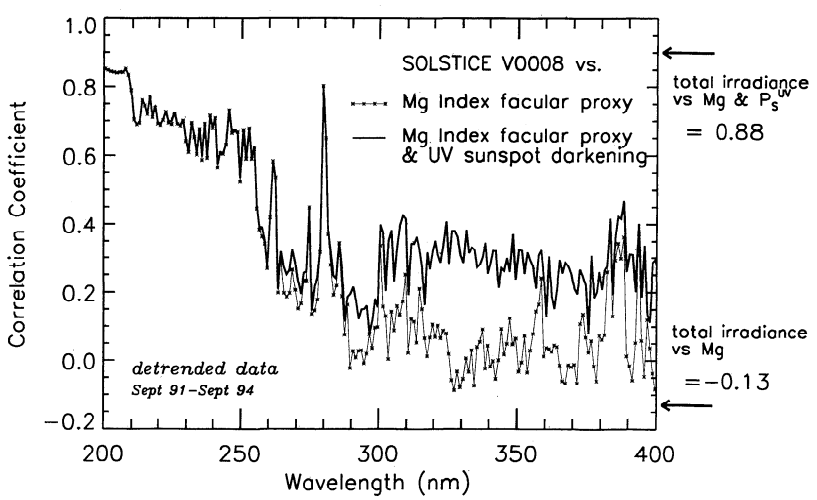

Figure 11. Correlation coefficients determined by linear regression of detrended SOLSTICE spectra in 1-nm bins with the detrended Mg II index facular proxy (thin line with asterisks) compared with correlation coefficients determined by multiple regression using detrended Mg II facular and sunspot darkening proxies (solid line). Including the sunspot darkening increases the correlation coefficients significantly at wavelengths longward of 300 nm, providing evidence for signatures of sunspot influences in the SOLSTICE 1-nm spectra. Also indicated by the arrows on the right-hand side are the correlation coefficients for total solar irradiance and the corresponding proxies.

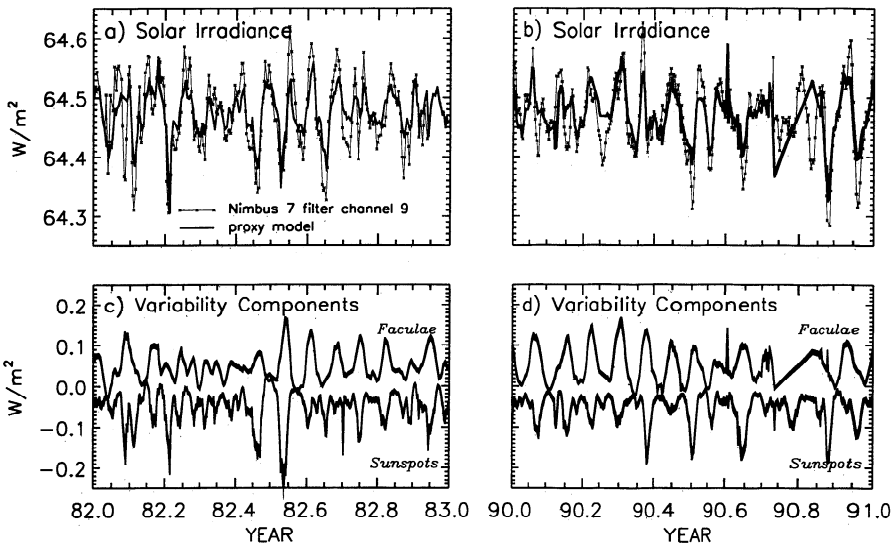

Figure 12. Corrected Nimbus 7 filter channel 9 signals (thin lines with asterisks) compared with reconstructions of the signals using sunspot and facular proxies in (a) 1982 and (b) 1990, with (c, d) the relative energy contributions by sunspot darkening and facular brightening that best match the variations present in the corrected signals. Two approaches (multiple regression of the corrected signals with detrended sunspot and facular proxies, and sunspot subtraction from the corrected signals followed by linear regression of the residual with the detrended facular proxy) were used to determine the relative sunspot and facular contributions, and the thickness of the solid line reflects the differences (which are minor) between these two approaches.

total signal within the filter passband, corrected for aspect, temperature and long term drifts by subtraction of a 35-day running mean, and ratioed to the data mean value. Figures 7g and 7h provide examples of the Nimbus filter channel signals corrected for aspect, temperature, and long-term drifts in this way. For the SOLSTICE data, $F(\lambda, t)$ is the irradiance in 1-nm bins on a 0.5-nm grid from 200 to 400 nm (i.e., a total of 200 individual time series) likewise detrended by subtracting 35-day running means and ratioing to the mean of the time series. Since the Nimbus 7 and SOLSTICE data have had long-term trends removed to avoid the confusion of real solar variability with instrumental sensitivity changes, long-term trends are similarly removed from both P_S^{320} and P_F^{PROX} prior to performing the linear regressions. Consequently, the coefficients, $a(\lambda)$, $b(\lambda)$, and $c(\lambda)$, deduced from the detrended solar data quantify variations only on short to intermediate timescales.

Figure 12 compares data from the two Nimbus 7 UV filter channels with the reconstructions deduced from multiple regression analysis (equation (6)). Correlation coefficients for the detrended channel 9 corrected signals and the proxy reconstructions are 0.77 in 1982 and 0.72 in 1990. Figure 13 compares the SOLSTICE variations in broad wavelength bands with their proxy reconstructions, determined from (6) separately for each 1-nm bin then integrated over the specified 50-nm wavelength bands. Correlation coefficients for the detrended SOLSTICE measurements shown in Figure 13 (176 days from November 1991 to May 1992) and their proxy reconstructions are 0.91, 0.55, 0.55, and 0.51 for the bands 200–250, 250–300, 300–350, and 350–400 nm, respectively. The decrease in correlation coefficient tracks the decrease in solar irradiance variability amplitude with increasing wavelength. Whereas rotational modulation of amplitude near 2% is evi-

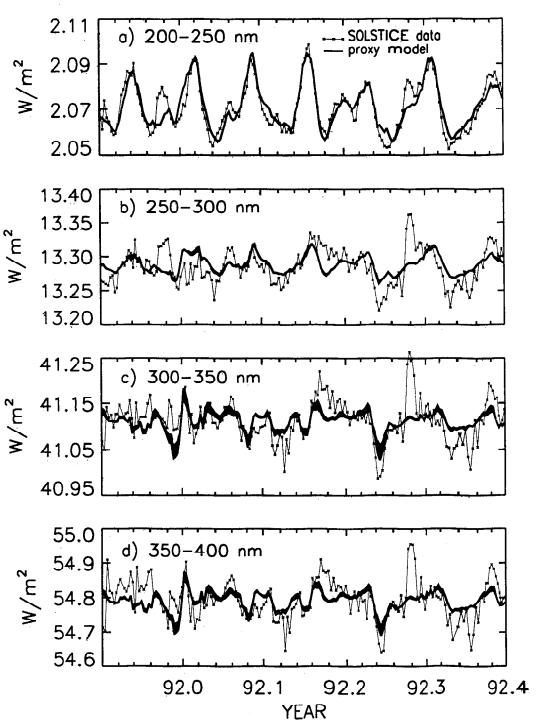

Figure 13. Irradiance reconstructions by a proxy facular/sunspot model (solid lines) compared with measurements of UV irradiance variations (thin lines with asterisks) obtained by summing the detrended SOLSTICE 1-nm spectra over the wavelength ranges (a) 200–250 nm, (b) 250–300 nm), (c) 300–350 nm and (d) 350–400 nm. The proxy reconstructions shown are determined analogously to the Nimbus 7 reconstructions in Figures 12a and 12b.

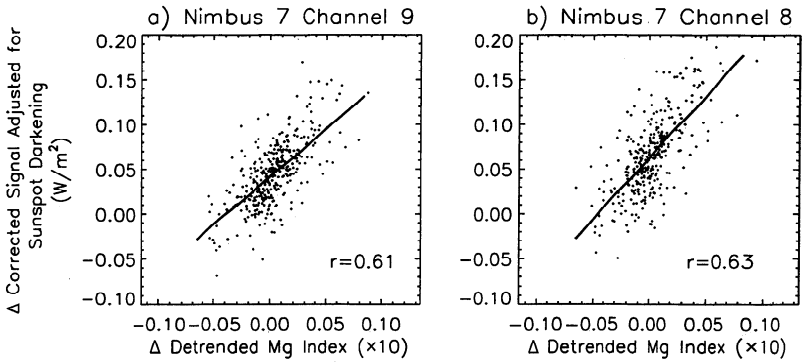

Figure 14. After removing the fully specified sunspot darkening contribution to the corrected Nimbus 7 filter channel signals, linear regressions of the residual variations with the residuals of the Mg II index facular proxy after detrending establish quantitatively the facular-related components in the data. Shown are scatter plots and correlation coefficients for Nimbus 7 filter channels (a) 9 and (b) 8 versus the proxy. Each plotted point is the average of 5 individual days.

dent in Figure 13 in the 200- to 250-nm band, the 250- to 300-nm band varies by 0.4%, and the 300- to 350-nm and 350- to 400-nm bands varies by about 0.2%. Since the UV spectrum variations detected at wavelengths longer than 250 nm are only of the order of SOLSTICE's short-term repeatability, instrumental effects dominate the variance in these data and reduce the correlation with the proxy parameterizations.

4.2. Sunspot Subtraction Approach

Because the sunspot and facular proxies are themselves correlated (correlation coefficient of 0.69 for 4295 daily observations from November 1978 to December 1994, in Figure 2), there is a potential for ambiguity in apportioning variance in the measured UV irradiances to sunspot and facular sources by multivariate regression. An alternative approach is to remove from the measured irradiances both the background irradiance and the directly specified sunspot darkening, then correlate the residual irradiances with a facular proxy. For a UV irradiance time series at a given wavelength, bivariate linear regression determines the coefficients $j(\lambda)$ and $k(\lambda)$ such that

$$F(\lambda, t)^{\mathrm{RES}} = F(\lambda, t) - F_{\mathrm{AV}}(\lambda) - F_{\mathrm{AV}}(\lambda) P_S^{\mathrm{UV}}(\lambda, t)$$
$$= j(\lambda) + k(\lambda) P_F^{\mathrm{PROX}}(t) \quad (7)$$

where $F_{\mathrm{AV}}(\lambda)$ is the mean level of the detrended irradiance, i.e., the background irradiance on which the short-term sunspot and facular perturbations occur.

Essential for the sunspot subtraction approach are absolute values of the sunspot darkening at all wavelengths and at all times of interest. In order to remove sunspot modulation of the Nimbus 7 filter data, effective sunspot contrasts C^{EFF} are evaluated for each filter using the filter transmittance $T(\lambda)$ and the average solar spectral irradiance $F_{\mathrm{AV}}(\lambda)$ (both shown in Figure 1), as

$$C^{\mathrm{EFF}} - 1 = \frac{\int [C_S^{\mathrm{ALLEN}}(\lambda) - 1] F_{\mathrm{AV}}(\lambda) T(\lambda)\, d\lambda}{\int F_{\mathrm{AV}}(\lambda) T(\lambda)\, d\lambda} \quad (8)$$

where the integration occurs over all wavelengths for which $T(\lambda)$ is nonzero. The results of evaluating (8) are $C^{\mathrm{EFF}} - 1 = -0.47$ for channel 9 and $C^{\mathrm{EFF}} - 1 = -0.45$ for channel 8. Figure 14 shows scatterplots of $F(t)^{\mathrm{RES}}$ and P_F^{PROX} for the two Nimbus 7 filter channels; linear regressions of these data yield values of j and k that allow reconstruction of the irradiance from the proxies via (7). Similarly, linear regressions of the SOLSTICE residuals with the Mg index facular proxy yield values of $j(\lambda)$ and $k(\lambda)$ for successive 1-nm bins from 200 to 400 nm. Figure 15 illustrates the regression for two such 1-nm bins. The irradiance residual in the 250.5-nm bin correlates strongly with the Mg index (correlation coefficient of 0.72), whereas for the 1-nm bin centered on 350.5 nm the correlation is much less (correlation coefficient of 0.13), signifying much weaker facular dependence at this wavelength.

For both the Nimbus 7 filter channels and the SOLSTICE spectra, the irradiances reconstructed from the sunspot subtraction approach agree well with independently reconstructed irradiances deduced from multiple regression fitting of sunspot and facular proxies. In the comparisons of the measured and reconstructed irradiances for the Nimbus and SOLSTICE data shown in Figures 12 and 13, respectively, the thickness of the solid line denoting the proxy model provides an indication of the range of values given by the two different reconstruction approaches. In all cases the differences between the two approaches is notably less than the differences between the proxy reconstructions and the data. As was discussed in section 4.1, measured and reconstructed irradiances agree better at the shorter mid-UV wavelengths, which vary by a few percent, than at longer near-UV wavelengths, whose variations of a few tenths percent are comparable to the short-term measurement repeatability.

5. Inferred 11-Year Cycle Amplitudes of Mid- and Near-UV Solar Radiation

Sunspot and facular influences on solar UV radiation change continuously throughout the 11-year solar cycle, as well as during the shorter-term solar rotation. The Sun's rotation on its axis, once approximately every 27 days, modulates solar irradiance by altering the earthward projection of inhomogeneously distributed radiation sources on its disk. Additional modulation occurs over the 11-year cycle as sunspots and faculae form, evolve, and decay in response to a net increase in the overall amount of magnetic flux in the Sun's atmosphere at solar activity maximum relative to activity minimum.

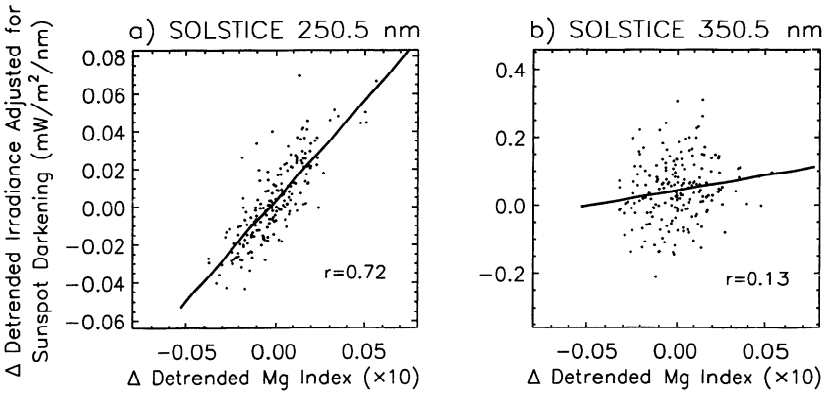

Figure 15. After removing sunspot darkening contributions to the detrended SOLSTICE 1 nm spectra, linear regressions of the residual variations with the residuals of the Mg II index facular proxy after detrending establish the spectrum of facular-related components on a 1 nm grid. Shown are scatter plots and correlation coefficients for SOLSTICE wavelengths (a) 250.5 nm and (b) 350.5 nm versus the proxy. In Figure 15a, changes in the 250.5-nm radiation exhibit a strong relationship with facular changes compared with the negligible correlation in Figure 15b at 350.5 nm. Each plotted point is the average of 5 individual days.

5.1. Reconstructions of Solar Cycle UV Irradiances

The parameterizations developed in the previous sections to reconstruct solar UV irradiance variations over predominantly rotational timescales permit estimation of solar cycle changes attributable to sunspot and facular influences by utilizing the longer-term proxy data sets that document these influences over the 11-year cycle. This approach assumes that sunspots and faculae modulate solar radiative output similarly over both short and long timescales. In support of this assumption, the same combination of bolometric sunspot darkening and a linear parameterization of the He EW facular proxy accounts for much of the variability in the total radiative output (dominated by radiation longward of 400 nm) recorded by the ACRIM SMM over both solar rotation and the solar cycle [*Foukal and Lean*, 1988; *Lean*, 1991; *Lean et al.*, 1995a]. Likewise, *Chandra et al.* [1995] demonstrate that the relationship between the Mg II index facular proxy and the 200-nm irradiance measured directly by SOLSTICE on UARS is similar whether deduced from solar rotational modulation or from the overall longer-term changes that occurred during the descending phase of solar cycle 22. Both the bolometric and UV studies thus suggest that the assumption of equivalent rotational and cyclic proxy scaling factors is probably valid for the mid- and near-UV spectrum but full verification requires additional long-term solar monitoring with improved long-term repeatability over longer time periods.

Figure 16 shows the variability during the past 17 years of solar UV radiation in four 50-nm wavelength bins from 200 to 400 nm, reconstructed from sunspot and facular proxies using the parameterizations deduced from multiple regression of the SOLSTICE rotationally modulated 1-nm spectra. In September 1986, the month of lowest activity during the minimum between solar cycles 21 and 22, $\langle P_S^{UV} \rangle = 15.58$ millionths of the solar hemisphere and $\langle P_F^{PROX} \rangle = 0.2635$. The month of strongest solar activity in solar cycle 22 is November 1989, for which $\langle P_S^{UV} \rangle = 1003.29$ millionths of the solar hemisphere and $\langle P_F^{PROX} \rangle = 0.2834$.

Table 1 provides numerical values for September 1986 and November 1989 of the UV energy (as well as ratios and dif-

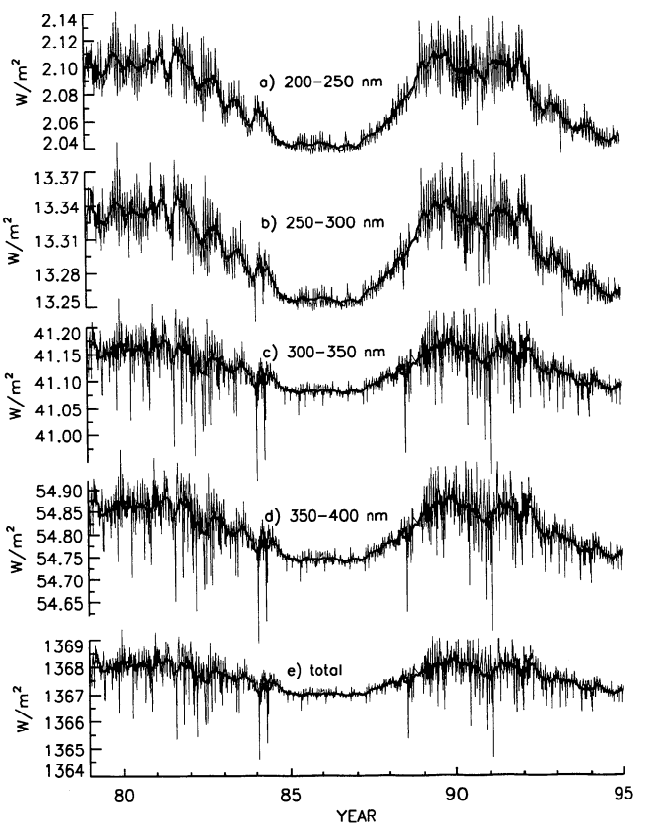

Figure 16. Solar mid- and near-UV irradiance variations reconstructed from 1979 to 1995 by using the sunspot darkening and facular brightening parameterizations deduced by multiple regression of the detrended SOLSTICE 1-nm spectra, summed into wavelength bands (a) 200–250 nm, (b) 250–300 nm, (c) 300–350 nm) and (d) 350–400 nm, with (e) variations in total radiative output, estimated from a proxy model of the SMM/ACRIM I measurements from 1980 to 1989 [*Lean et al.*, 1995a], shown for comparison. According to the solar activity proxies, minimum solar activity between solar cycles 21 and 22 occurred in September 1986, while November 1989 was the month of maximum activity in solar cycle 22.

Table 1. Solar UV Energy in Specified Wavelength Bands Averaged During September 1986 (Solar Minimum) and November 1989 (Solar Maximum)

Wavelength Band, nm	SEP86 W/m^2	NOV89 W/m^2	NOV89/SEP86	NOV89 − SEP86, W/m^2	Percent of ΔS [NOV89 − SEP86]/1.34 × 100
200–250	2.037	2.113	1.0369	0.075	5.6
250–300	13.251	13.348	1.0074	0.098	7.3
300–350	41.076	41.172	1.0023	0.096	7.2
350–400	54.737	54.881	1.0026	0.144	10.7
200–300	15.288	15.461	1.0113	0.173	12.9
300–400	95.813	96.053	1.0025	0.240	17.9
200–400	111.101	111.514	1.0037	0.413	30.8

Here SEP86 and NOV89 denote September 1986 (solar minimum) and November 1989 (solar maximum) average UV energy, respectively. Ratios and differences of these averages provide estimates of the UV irradiance variability during the 11-year solar activity cycle. Note that the mean activity level during September 1986 is slightly higher than the true "quiet" Sun realized on those days when all active regions are absent from the disk entirely (the latter is used by *Lean et al.* [1995b] to signify true solar minimum conditions). Also provided are the energies in the bands as fractions of the ΔS = 1.34 W/m^2 energy change in total radiative output over the same period, estimated from a reconstruction of the SMM/ACRIM I measurements [*Lean et al.*, 1995a].

ferences of these values) divided into four 50-nm bins and two 100-nm bins and for the entire interval from 200 to 400 nm. According to the estimates in Table 1, the entire solar UV radiation from 200 to 400 nm increased 0.37% during the recent solar cycle because the enhanced UV radiation from faculae more than compensated the radiation deficit in sunspots. Radiation in the 200- to 250-nm band increased by 3.7%, with smaller increases of 0.7% in the 250- to 300-nm band, and 0.23% and 0.26% in the 300- to 350-nm and 350- to 400-nm bands, respectively.

Whereas Figure 16 provides the detailed temporal fluctuations of reconstructed solar UV radiation in four broad wavelength bands arising from sunspot and facular influences over the past few decades, Figure 17 shows the detailed wavelength dependence (at 1-nm resolution) of the spectral changes from cycle minimum (September 1986) to maximum (November 1989). Both the energy increases and the ratios of cycle maximum and minimum spectra have considerable spectral structure that corresponds closely with absorption and ionization features in the actual solar irradiance. This matching of spec-

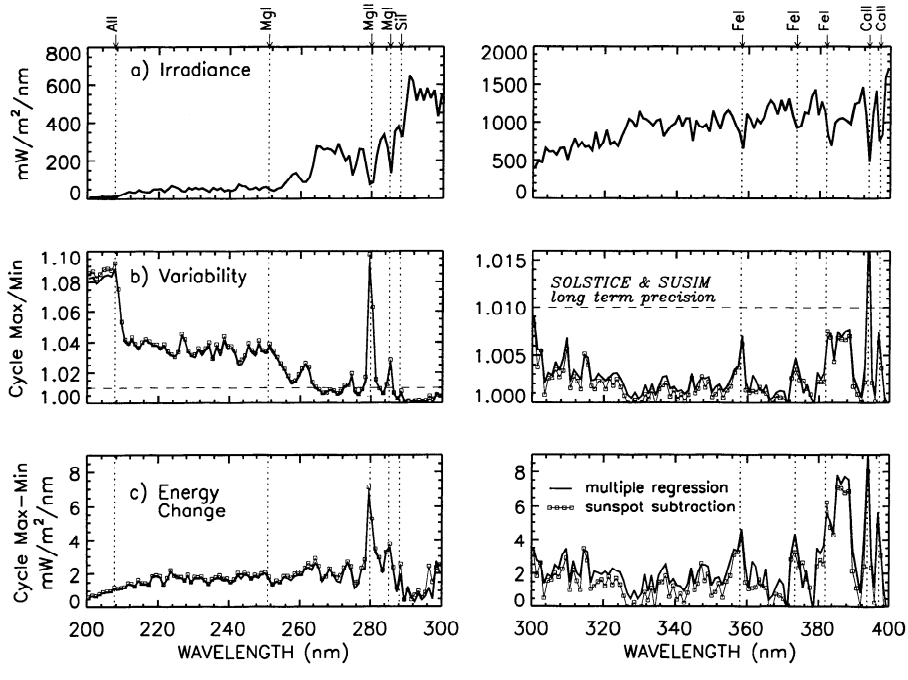

Figure 17. (a) SOLSTICE solar spectral irradiance from 200 to 400 nm, in 1-nm bins. (b) Ratios of the spectral irradiance in November 1989 (solar maximum levels) and September 1986 (solar minimum levels) determined from the proxy irradiance model, giving estimates of the spectrum variations during the 11-year solar activity cycle. The long dashed horizontal line indicates the long-term repeatability goal of the SOLSTICE measurements. (c) Changes in spectral energy from maximum to minimum solar activity levels. The dotted vertical lines and the corresponding arrows along the top panel identify the wavelengths and origins of primary spectral features.

Table 2. Comparison of Solar Cycle Irradiance Variations Determined From Independent Parameterizations of the Nimbus 7 and SOLSTICE Rotationally Modulated Data, Using Both Multiple Regression and the Sunspot Subtraction Approaches

Data	Analysis Technique	Change, %	
		Filter Channel 9 (275–360 nm)	Filter Channel 8 (300–410 nm)
Nimbus 7 corrected filter channel signals	multiple regression analysis	0.24	0.18
	sunspot subtraction approach	0.23	0.19
SOLSTICE spectra convolved with filter transmittance	multiple regression analysis	0.26	0.21
	sunspot subtraction approach	0.21	0.15
Mean ± standard deviation		0.24 ± 0.02	0.18 ± 0.03

Percentage changes from the maximum to minimum of the 11-year solar cycle are determined as [NOV89/SEP86 − 1] × 100, where NOV89 is the average irradiance value for November 1989 (cycle 22 maximum activity) and SEP86 is the average irradiance value for September 1986 (cycle 21–22 activity minimum). To facilitate a direct comparison with the estimates derived from the Nimbus 7 broadband filter channels, the SOLSTICE 1-nm spectra are convolved with the respective channel 9 and channel 8 filter transmittance functions, shown in Figure 1.

tral shapes among the three different panels in Figure 17 gives confidence that the displayed spectral features are attributable to real solar variability, rather than simply to noise arising from uncertainties in the proxy parameterizations, traceable to inadequate short-term SOLSTICE measurement repeatability.

Marked irradiance increases and variability decreases occur near the Al I ionization edge at 207.5 nm and the Mg I edge near 251 nm. Radiation longward of these features emerges from progressively lower layers of the Sun's photosphere [*Vernazza et al.*, 1976]. Similarly, emissions in the cores of the Fraunhofer absorption lines (whose wavelengths and species are identified by arrows in Figure 1 and 17) emerge from higher layers of the photosphere and chromosphere and vary more than radiation at adjacent wavelengths, emitted as part of the underlying blackbody continuum. In fact, the entire near-UV spectrum from 300 to 400 nm is a complex mix of continuum emission and absorption by predominantly Mg I, Mg II, Ca II, and Fe [*Kuruz*, 1992], and the variability ratios reflect closely this complex structure, even at the modest 1-nm resolution of the SOLSTICE data.

The reconstructed broadband UV irradiance time series in Figure 16 and the 1-nm spectrum changes in Figure 17 were determined from parameterizations deduced from multiple linear regression of sunspot and facular proxies with the SOLSTICE rotationally modulated irradiances (section 4.1). Also provided in Figure 17 are the solar cycle spectrum changes deduced by first subtracting the calculated sunspot darkening from the SOLSTICE spectra (section 4.2). Both the multiple regression and sunspot subtraction approaches yield similar estimates of the spectral irradiance variations. As a further metric of the uncertainties associated with the results from the two different approaches, and with using SOLSTICE versus Nimbus 7 data, Table 2 compares estimates of the solar cycle percentage changes (from September 1986 to November 1989) deduced from the SOLSTICE 1-nm spectra and independently from the two Nimbus 7 filter channels using both approaches. To facilitate this comparison, the SOLSTICE maximum and minimum spectra were convolved with the Nimbus 7 filter channel transmittance given in Figure 1, so that the variations listed in Table 2 pertain specifically to the radiation corresponding to the Nimbus 7 filter channels 9 (275–360 nm) and 8 (300–410 nm). Consistent with the expectation of smaller variability in longer wavelength radiation, all four approaches indicate less variability in the longer-wavelength filter channel 8 (0.18%) than in filter channel 9 (0.24%). The data in Table 2 indicate that for each of the two filter channels, results from the multiple regression analysis of the SOLSTICE spectra are consistent with the mean of the four estimates, validating their use in Figures 16 and 17. The standard deviations of the four different determinations (two separate approaches for each of the Nimbus 7 and SOLSTICE observations) are 8% for channel 9 and 17% for channel 8, which provide a semiquantitative measure of the range of uncertainties likely associated with the variability ratios in Table 1.

At wavelengths less than 300 nm, where facular influences dominate emission variability, there is very good agreement between the solar cycle spectral irradiance changes deduced from the sunspot and facular parameterizations shown in Figure 17 and solar cycle irradiance changes based on composite Mg index scaling factors deduced independently from SBUV data (i.e., from parameterizations using a facular proxy alone) [*DeLand and Cebula*, 1993, 1997]. Figure 18 illustrates this agreement. However, our multiple regression parameterization predicts larger variations in the near UV spectrum from 300 to 400 nm than does the DeLand and Cebula facular scaling. Whereas our results indicate that the entire mid and UV spectral irradiance increases from solar cycle minimum to maximum, the DeLand and Cebula analysis is consistent, within their error bars, with no solar cycle change in radiation from 290 to 400 nm except in the cores of the Ca II *H* and *K* lines. Their lack of inclusion of sunspot influences is the reason for this discrepancy. Interestingly, both solar cycle estimates shown in Figure 18 do exhibit similar spectral details throughout the entire mid- and near-UV spectrum, indicating the potential for the detection of real mid-UV variability in the SBUV data.

At wavelengths longward of about 250 nm, exclusive of the cores of some Fraunhofer lines, the solar cycle variations indicated in Figure 17 are of the order of, or less than, the ±1% long-term repeatability of state-of-the-art solar UV monitors and thus cannot be validated by direct observations. With this caveat, Figure 19 compares reconstructed irradiances with direct observations during the past 2 decades. In the 200- to 250-nm band, for which the solar cycle amplitude is estimated to be 3.7%, the reconstructed irradiances overestimate slightly the variability measured by SOLSTICE but underestimate the variability measured concurrently by the Solar Ultraviolet Spectral Irradiance Monitor (SUSIM), also on UARS. Variations reconstructed in the three longer-wavelength bands show considerably less variability than do the observations, among which there are significant discrepancies, presumably of instrumental origin. However, SOLSTICE observations in the 300- to 350-nm band, for which short-term noise is less than in the

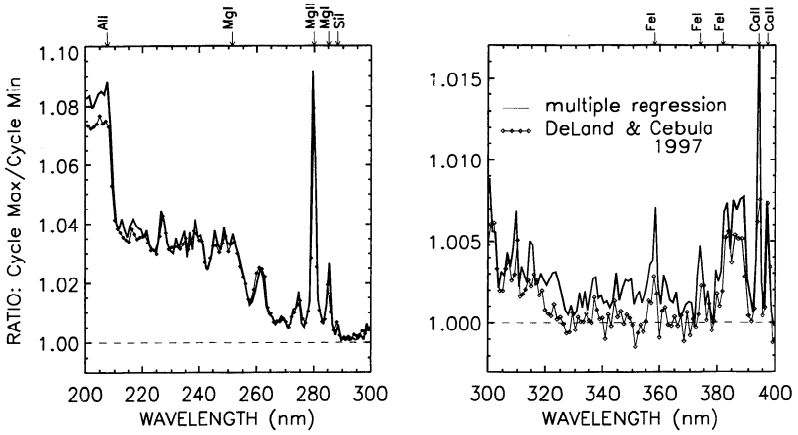

Figure 18. Estimates of mid- and near-UV solar spectral irradiance change from the minimum (September 1986) to the maximum (November 1989) of the solar activity cycle. The solid line indicates the estimates determined from the facular and sunspot multiple regression analysis, shown in Figure 17, and the diamonds connected by the thin line are deduced independently by scaling the rotational modulation measured by the Solar Backscatter Ultraviolet experiments with the Mg II index facular index, alone, determined from the NOAA 9 data [*DeLand and Cebula*, 1993, 1997].

two adjoining bands, show surprisingly good agreement with the reconstructed irradiance. This suggests that refinement of long-term trends in SOLSTICE data may yield improved agreement between the measured and reconstructed irradiances in other wavelengths bands as well. An effort is presently under way to revise the algorithm that defines the SOLSTICE stellar pointing with the goal of increasing the repeatability of mid- and near-UV irradiances.

5.2. Comparison of UV and Total Irradiance Variabilities

Reconstruction of the 200- to 400-nm UV radiation determined from multiple regression of sunspot and facular proxies with the SOLSTICE radiometry predicts an energy increase from 111.1 W/m^2 at solar cycle minimum to 111.5 W/m^2 at cycle maximum (Table 1). Although 111 W/m^2 is only 8% of the Sun's 1367 W/m^2 total radiative output, the energy change of 0.41 W/m^2 in the entire 200- to 400-nm band accounts for almost 31% of the 1.34 W/m^2 total irradiance cycle. The estimated total radiative output change of 1.34 W/m^2 which, like the UV energy change, is the increase from September 1986 to November 1989, is based on a reconstruction of ACRIM I observations from 1980 to 1989 using bolometric sunspot darkening and the Mg II index (or the He EW) facular proxy, following the approach of *Foukal and Lean* [1988, 1990], updated by *Lean et al.* [1995a].

Of the UV radiation from 200 to 400 nm, the Earth's atmosphere absorbs essentially all that at wavelengths shortward of 310 nm (Figure 1). Figure 20 shows the estimated variations in the solar energy longward of 310 nm that can reach the Earth's surface, determined by subtracting the total energy at 200–310 nm from the total radiative output, where each time series is reconstructed from sunspot and facular components. Figure 20 also shows the solar cycle changes estimated to occur in the UV energy from 200 to 310 nm relative to the total radiative output. These variations demonstrate that the relationship between solar energy that is absorbed in the Earth's atmosphere and that penetrates to its surface is not constant. Rather, variations in this relationship occur because facular effects dominate the shorter wavelength UV radiation whereas sunspots contribute more significantly to modulation of the total radiation.

6. Discussion

Our new quantitative estimates of 11-year cycle variations in the Sun's 1-nm spectrum from 200 to 400 nm extend knowledge of the Sun's spectral irradiance variations to wavelengths

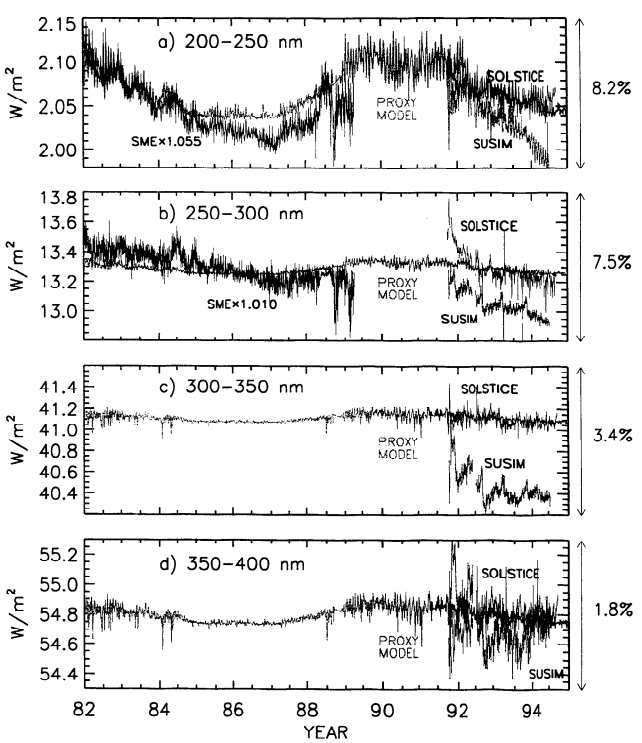

Figure 19. Time series of solar UV irradiances reconstructed from proxy sunspot-facular models (shown as the gray lines) compared with available irradiance observations in broad bands at (a) 200–250 nm, (b) 250–300 nm, (c) 300–350 nm, and (d) 350–400 nm. The irradiance measurements were made by the Solar Mesosphere Explorer (SME) [*Rottman*, 1988] in solar cycle 21, with the absolute irradiance scale adjusted as indicated, and by the SOLSTICE and SUSIM on UARS in solar cycle 22 [*Woods et al.*, 1996].

longward of 300 nm by accounting for both sunspot and facular influences where previously less robust analyses derived from scalings of facular influences alone. Direct measurements of long-term changes in most of the Sun's spectrum are not possible using existing solar monitors, including the state-of-the-art instruments on UARS. Cavity radiometers such as ACRIM monitor the total (i.e., spectrally integrated) solar radiative output with long-term repeatability of a few hundredths of a percent but lack the sensitivity to reliably detect the much smaller signals in wavelength bands of even broad width. Although sufficiently sensitive, spectral irradiance monitors such as SOLSTICE and SUSIM have long-term repeatabilities that are poorer by a factor of 100 than ACRIM's and exceed the actual solar spectrum changes at all but UV wavelengths shortward of about 250 nm. Our parameterizations of the solar mid- and near-UV spectrum variations, focusing on short to intermediate rotational timescales to eliminate unspecified long-term instrument sensitivity change, are made possible because the short-term repeatability of the SOLSTICE measurements approaches at times a few tenths of a percent, which is comparable to the irradiance modulation by solar rotation.

Conceptually, the solar cycle amplitudes of 1.1% and 0.25% for mid-UV radiation from 200 to 300 nm and near-UV radiation from 300 to 400 nm, respectively, are consistent with the present broad understanding of solar spectrum variability decreasing in amplitude as wavelength increases from the UV to the visible. Shorter wavelength mid-UV radiation varies more than near-UV emission, and both UV bands vary more than the 0.1% cycle in total radiative output, composed primarily of longer wavelength radiation. Similarly, the temporal character of the reconstructed irradiances conforms closely to independent evidence for facular domination of shorter UV wavelengths, formed generally higher in the Sun's photosphere, and combined sunspot and facular influences on total radiative output. Our reconstructions document the transition from facular dominance to competing sunspot and faculae influences across the region 200 to 400 nm, which lies between the UV and visible spectrum, and are consistent with independent determination of the wavelength dependence of the sunspot darkening.

Solar radiation variability exhibits significant spectral structure throughout the UV region, with a marked change in character near 300 nm. Facular effects dominate the short-, intermediate-, and long-term variations in the radiation from 200 to about 300 nm, whereas radiation from 300 to 400 nm exhibits significant short-term sunspot-related depletions and is thus more similar in character to total radiative output variations, although as for total radiative output, faculae control the overall solar cycle modulation. This transition in temporal structure near 300 nm mimics a transition of physical radiative processes within the Sun's atmosphere. Whereas opacity by H^- dominates longer wavelength radiation, multiple lines contribute to the opacity at shorter wavelengths. Consequently, radiation from about 300 to 1000 nm emerges from approximately similar heights within the Sun's atmosphere, near that of unit optical depth for 500-nm radiation, with brightness temperatures near 6000 K, but shorter wavelength radiation in the region 200–300 nm is formed at increasing cooler temperatures and higher layers of the Sun's photosphere [*Vernazza et al.*, 1976]. The mid- and near-UV radiation bands undergo energy changes of 0.17 W/m^2 and 0.24 W/m^2 during the solar cycle and contribute about 13% and 18%, respectively, to the total radiative output variability.

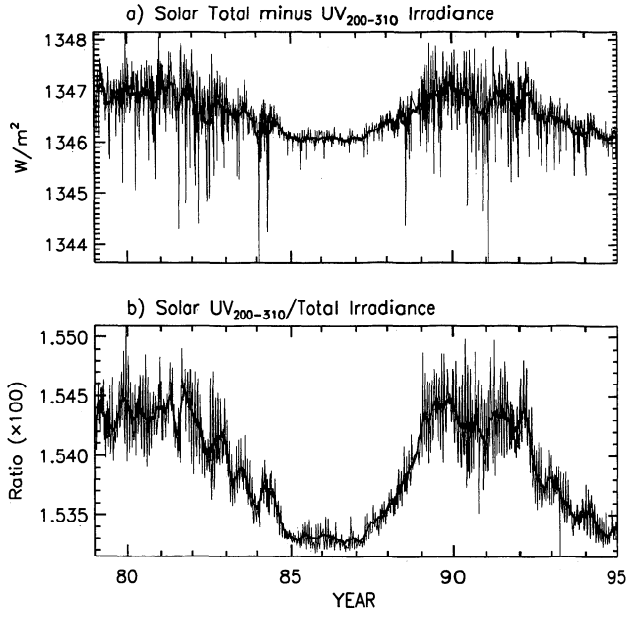

Figure 20. (a) Reconstruction of the Sun's total irradiance minus the UV radiation from 200–310 nm. Since the Earth's atmosphere absorbs UV radiation shorter than 310 nm, this part of the solar spectrum is unavailable for direct heating of the Earth's surface. Removing the UV component of solar radiation from the total irradiance thus provides a geophysical quantity of different climatic relevance than total irradiance, alone. (b) Ratios of the UV and total irradiances, indicating that the relationship of these two quantities itself varies over the solar cycle.

Distinct features in the reconstructed solar spectrum variability match closely features in the actual solar spectrum and are related to absorption and ionization of atomic species present in the Sun's atmosphere. The cores of all the strong Fraunhofer lines throughout the 300- to 400-nm spectrum vary significantly more than does radiation from the wings of the lines and the nearby underlying continuum. In some selected wavelengths that approach true continuum emission (for example, near 330, 373, and 379 nm), solar cycle variations are of the order of 0.1% or less. Independent solar monitoring of certain spectral features with much higher spectral resolution indicates even greater emission variations in line cores. For example, the core of the Ca II *K* line near 390 nm, seen in Figure 17 to vary by about 1.5% over the 11-year solar cycle, varies by 10 times more when monitored with 10 times higher resolution [*White et al.*, 1990]. This raises the possibility that solar spectrum changes occur primarily in spectral lines, perhaps at a greater level than a recent estimate of 20% [*Ulrich and Bertello*, 1995].

Although direct solar monitoring cannot validate our long-term variability estimates, comparison of our reconstructed solar cycle changes with directly measured total radiative output variations does provide some constraint on the magnitude of UV irradiance variability. By our estimate, the 0.37% variation in the entire wavelength band from 200 to 400 nm contributes almost one third of the total radiative output cycle. Were the entire total irradiance change attributable to UV radiation, alone, the variability amplitude of the 200- to 400-nm spectrum would thus be limited to 3 times its presently estimated value, i.e., to less than about 1%. However, Nimbus

7 filter channels longward of 400 nm and recent Solar and Heliospheric Observatory (SOHO) observations of visible and near-IR radiation [*Fröhlich et al.*, 1997] provide strong evidence for solar spectrum variability at wavelengths longward of 400 nm, thereby reducing further the 1% upper limit of the 200- to 400-nm irradiance variability amplitude. Preliminary analysis suggests, for example, that the 698- to 2800-nm Nimbus 7 filter channel alone may account for about one third of the total radiative output changes. In this context, improved quantitative definition of the variability of the visible and infrared spectrum may well provide a tighter constraint on the upper limit of the UV irradiance changes than can the direct UARS observations with maximum ±1% long-term repeatability. The technique which we have used here, of modeling observed rotationally modulated data using sunspot and facular proxies, is equally applicable to other spectral regions and is being used to similarly interpret changes in Nimbus 7 filter channels at visible and near-IR wavelengths, with the goal of eventually determining spectral variability at all wavelengths. Analysis of solar monitoring by the Variability of Solar Irradiance and Gravity Oscillations (VIRGO) instrument on SOHO [*Fröhlich et al.*, 1995, 1997] and the Global Ozone Monitoring Experiment (GOME) [*Weber et al.*, 1997; K. Chance, private communication, 1996] will likewise contribute to better definition of visible and infrared spectral irradiance variations.

The capability of reconstructing solar spectrum changes in any selected spectral region afforded by the newly developed parameterizations provides a flexibility that may improve simulations of climate response to solar forcing. Our parameterizations enable the reconstruction of solar energy inputs in wavelength bands tailored to reflect the relevant physical processes. As an example, a newly developed coupled ocean atmosphere model is presently being used at the Goddard Institute of Space Studies to simulate the response of climate to solar and other forcings during the last 15 years, using three solar inputs: 200–295 nm (stratosphere), 295–315 nm (troposphere) and total radiative output, deduced from our sunspot and facular parameterizations (J. Hansen, private communication, 1996). More generally, knowledge of the Sun's spectral irradiance variations at all wavelengths is a key requirement for investigating the physical processes by which variable solar radiation interacts with the Earth's environment, thereby contributing natural variability to the climate and atmosphere. Our estimates extend this knowledge to 400 nm, but additional effort is required to determine spectrum changes at longer wavelengths still.

Accomplishing the needed long-term repeatability in future solar monitoring will require improved or new types of solar spectrum monitors with long-term repeatability better than 0.1%. One approach is to forgo higher spectral resolution for radiometric stability using broadband devices analogous to the Nimbus 7 filter channels. A new generation of space-hardened transmittance filters can afford improved long-term stability of broadband filter radiometers and multiple detectors can provide in-flight sensitivity tracking similar to the approach employed successfully by ACRIM. Also under consideration is improvement of the in-flight sensitivity tracking using bright blue stars and use of on-board standards. The parameterizations deduced here will be useful for comparisons with UARS solar irradiance monitoring in the immediate future and monitoring in the twenty-first century by the National Polar-orbiting Operational Environmental Satellite System (NPOESS) and the Earth Observing System (EOS). A particular challenge will be to ascertain from future solar monitoring the validity of the assumed equivalence of short- and long-term scalings between proxies and irradiances on which these parameterizations are based.

7. Summary

Solar magnetic activity modulates the solar mid- and near-UV radiation at wavelengths throughout the 200- to 400-nm spectrum. Sunspots and faculae are the prime causes of this modulation, consistent with the known sources of both longer- and shorter-wavelength solar irradiance variability. On the basis of parameterizations of these effects detected over predominantly rotational timescales, domination of faculae brightening over sunspot darkening on longer timescales causes the entire mid- and near-UV spectrum to increase during times of high solar activity, relative to solar minimum conditions. The deduced variations are conceptually consistent in amplitude and temporal structure with observed variations at both longer and shorter wavelengths. Near 300 nm there is a distinct change in the character of the variability. Whereas faculae provide the dominant modulation over both rotational and 11-year timescales for radiation at wavelengths shorter than 300 nm, the 300- to 400-nm radiation behaves more like the total solar irradiance, having distinct sunspot influences during short timescales. Largest modulation of the 300- to 400-nm spectrum occurs at wavelengths that correspond to the cores of Fraunhofer lines, for which cycle amplitudes range from 0.5% to 1.5% when studied at the 1-nm resolution of the SOLSTICE data. Less variability (of the order of 0.1–0.2%) is evident at other wavelengths in the wings of these lines. Whether solar radiation variations are truly confined to and dominated by the spectral lines is not presently known, and this determination is beyond the detection limitations of the present analysis of 1-nm-resolution spectra.

Reconstructions of long-term solar spectrum variations based on sunspot and facular records indicate an increase of 1.1% and 0.25% in respectively the 200–300 and 300–400 nm bands. For comparison, earlier, less rigorous estimates are 0.85% and 0.09% for these same bands [*Lean*, 1989]. The total 200- to 400-nm energy increases 0.4 W/m^2 from the minimum to the maximum of the recent 11-year solar cycle. This energy accounts for almost 31% of the Sun's total radiative output cycle, where the total irradiance change of 1.34 W/m^2 is determined from modelling the ACRIM SMM data using the approach of *Foukal and Lean* [1988, 1990].

Present observations are unable to confirm or refute our reconstructions of solar cycle irradiance changes except in the 200- to 250-nm region, where the average UARS changes are in generally good agreement with the reconstructed irradiances. Additional comparisons await further processing of the UARS data, which is in progress to identify and remove changes in the signals associated with instrumental effects.

Acknowledgments. Many people in the solar-monitoring community kindly aided in accessing the various databases needed for this work. Barry Knapp helped in obtaining and explaining the Solar Mesosphere Explorer data, and Doug Hoyt helped with accessing the Nimbus 7 filter channel data and their aspect and temperatures. Gérard Thuillier kindly provided SOLSPEC data. The SOLSTICE data are archived by the GSFC DAAC, whose personnel were very helpful in acquiring and reading the data files. Claus Fröhlich stressed the need to calculate a UV sunspot-darkening term. The NOAA WDC archives the sunspot region data used to calculate the UV sunspot-

blocking function; Helen Coffey has provided continual support in accessing these data. Rich Cebula and Matt DeLand provided their most recent Mg index time series and scaling factors for comparison with our results. A NASA UARS GI grant funded this work. Two reviewers provided extensive constructive comments.

References

Allen, C. W., *Astrophysical Quantities*, 3rd edition, Athlone, London, 1981.

Balachandran, N. K., and D. Rind, Modeling the effects of UV variability and the QBO on the troposphere-stratosphere system, I, The middle atmosphere, *J. Clim.*, *8*, 2058–2079, 1995.

Brandt, P. N., M. Stix, and H. Weinhardt, Modelling solar irradiance variations with an area dependent photometric sunspot index, *Sol. Phys.*, *152*, 119–124, 1994.

Brasseur, G., The response of the middle atmosphere to long-term and short-term solar variability: A two-dimensional model, *J. Geophys. Res.*, *98*, 23,079–23,090, 1993.

Brueckner, G. E., K. L. Edlow, L. E. Floyd, J. L. Lean, and M. E. VanHoosier, The solar ultraviolet spectral irradiance monitor (SUSIM) experiment onboard the Upper Atmosphere Research Satellite, *J. Geophys. Res.*, *98*, 10,695–10,711, 1993.

Cebula, R. P., M. T. DeLand, and B. M. Schlesinger, Estimates of solar variability using the solar backscatter ultraviolet (SBUV) 2 Mg II index from the NOAA 9 satellite, *J. Geophys. Res.*, *97*, 11,613–11,620, 1992.

Cebula, R. P., G. O. Thuillier, M. E. VanHoosier, E. Hilsenrath, M. Herse, G. E. Brueckner, and P. C. Simon, Observations of the solar irradiance in the 200–350 nm interval during the ATLAS-1 mission: A comparison among three sets of measurements—SSBUV, SOLSPEC, and SUSIM, *Geophys. Res. Lett.*, *23*, 2289–2292, 1996.

Chandra, S., and R. D. McPeters, The solar cycle variation of ozone in the stratosphere inferred from Nimbus 7 and NOAA 11 satellites, *J. Geophys. Res.*, *99*, 20,665–20,671, 1994.

Chandra, S., J. L. Lean, O. R. White, D. K. Prinz, G. R. Rottman, and G. E. Brueckner, Solar UV irradiance variability during the declining phase of solar cycle 22, *Geophys. Res. Lett.*, *22*, 2481–2484, 1995.

Chapman, G. A., A. D. Herzog, D. E. Laico, J. K. Lawrence, and M. S. Templer, Photometric measurements of solar irradiance variations due to sunspots, *Astrophys. J.*, *343*, 547–553, 1989.

DeLand, M. T., and R. P. Cebula, The composite Mg II solar activity index for solar cycles 21 and 22, *J. Geophys. Res.*, *98*, 12,809–12,823, 1993.

DeLand, M. T., and R. P. Cebula, Solar UV activity at solar cycle 21 and 22 minimum from NOAA-9 SBUV/2 data, *Sol. Phys.*, in press, 1997.

de Toma, G., O. R. White, B. G. Knapp, G. J. Rottman, and T. N. Woods, Mg II core-to-wing index: Comparison of SBUV 2 and SOLSTICE time series, *J. Geophys. Res.*, *102*, 2597–2610, 1997.

Donnelly, R. F., The solar Mg II core-to-wing ratio from the NOAA 9 satellite during the rise of solar cycle 22, *Adv. Space Res.*, *8*(7), 77–80, 1988a.

Donnelly, R. F., Uniformity in solar UV flux variations important to the stratosphere, *Ann. Geophys.*, *6*, 417–424, 1988b.

Donnelly, R. F., and L. C. Puga, Thirteen-day periodicity and the center-to-limb dependence of UV, EUV and X-ray emission of solar activity, *Sol. Phys.*, *130*, 369–390, 1990.

Fleming, E. L., S. Chandra, C. H. Jackman, D. B. Considine, and A. R. Douglass, The middle atmosphere response to short and long term solar UV variations: Analysis of observations and 2D model results, *J. Atmos. Terr. Phys.*, *57*, 333–365, 1995.

Foukal, P., Sunspots and changes in the global output of the Sun, in *The Physics of Sunspots*, edited by L. E. Cram and J. H. Thomas, p. 391, Sacramento Peak Observ., N. M., 1981.

Foukal, P., The behavior of solar magnetic plages measured from Mt. Wilson observations between 1915–1984, *Geophys. Res. Lett.*, *23*, 2169–2172, 1996.

Foukal, P., and J. Lean, Magnetic modulation of solar luminosity by photospheric activity, *Astrophys. J.*, *328*, 347–357, 1988.

Foukal, P., and J. Lean, An empirical model of total solar irradiance variation between 1874 and 1988, *Science*, *247*, 556–558, 1990.

Foukal, P., K. Harvey, and F. Hill, Do changes in the photospheric magnetic network cause the 11-year variation of total solar irradiance?, *Astrophys. J.*, *383*, L89, 1991.

Fröhlich, C., Irradiance observations of the Sun, in *The Sun as a Variable Star*, *IAU Colloq. 143*, edited by J. M. Pap et al., pp. 28–36, Cambridge Univ. Press, New York, 1994.

Fröhlich, C., J. M. Pap, and H. S. Hudson, Improvement of the photometric sunspot index and changes of the disk-integrated sunspot contrast with time, *Sol. Phys.*, *152*, 111–118, 1994.

Fröhlich, C., et al., VIRGO: Experiment for helioseismology and solar irradiance monitoring, *Sol. Phys.*, *162*, 101–128, 1995.

Fröhlich, C., D. A. Crommelynck, C. Wehrli, M. Anklin, S. DeWitte, A. Fichot, W. Finsterle, A. Jiménez, A. Chevalier, and H. Roth, In-flight performance of the VIRGO solar irradiance instrument on SOHO, *Sol. Phys.*, in press, 1997.

Haigh, J. D., The role of stratospheric ozone in modulating the solar radiative forcing of climate, *Nature*, *370*, 544–546, 1994.

Haigh, J. D., The impact of solar variability on climate, *Science*, *272*, 981–984, 1996.

Harvey, J. W., and W. C. Livingston, Variability of the solar He I 10830 Å triplet, in *International Astronomical Union Symposium 154: Infrared Solar Physics*, edited by D. M. Rabin, J. T. Jefferies and C. Lindsey, pp. 59–64, Kluwer Acad., Norwell, Mass., 1994.

Harvey, K., and O. R. White, Solar magnetic fields: The key to understanding solar irradiance variations, *Tech. Rep. 96-01*, Solar Phys. Res. Corp., 1996.

Heath, D. F., A review of observational evidence for short and long term ultraviolet flux variability of the Sun, in *Sun and Climate*, edited by R. Kandel, pp. 447–471, Cent. Natl. d'Etudes Spatiales, CNES, Toulouse, France, 1980.

Heath, D. F., and B. M. Schlesinger, The Mg 280-nm doublet as a monitor of changes in solar ultraviolet irradiance, *J. Geophys. Res.*, *91*, 8672–8682, 1986.

Hickey, J. R., Passive exposure of earth radiation budget experiment components LDEF experiment A0-147: Post flight examination and tests, in *LDEF—69 Months in Space, First Retrieval Symposium*, *NASA Conf. Publ.*, *3134*(3), 1493–1509, 1991.

Hickey, J. R., B. M. Alton, F. J. Griffin, H. Jacobowitz, P. Pellegrino, and R. H. Maschhoff, Indications of solar variability in the near UV from the Nimbus 7 ERB experiment, in *A Collection of Extended Abstracts Presented at the Symposium on the Solar Constant and the Spectral Distribution of Solar Irradiance*, *IAMAP Third Scientific Assembly, 17–28 August 1981, Hamburg*, edited by J. London and C. Fröhlich, Int. Assoc. of Meteorol. and Atmos. Phys., Boulder, Colo., 1982.

Hood, L. L., The solar cycle variation of total ozone: Dynamical forcing in the lower stratosphere, *J. Geophys. Res.*, *102*, 1355–1370, 1997.

Hood, L. L., J. Jirikowic, and J. P. McCormack, Quasi-decadal variability of the stratosphere: Influence of long term solar ultraviolet variations, *J. Atmos. Sci.*, *50*, 3941–3958, 1993.

Hoyt, D. V., H. L. Kyle, J. R. Hickey, and R. H. Maschhoff, The Nimbus 7 solar total irradiance: A new algorithm for its derivation, *J. Geophys. Res.*, *97*, 51–63, 1992.

Huang, T. Y., and G. P. Brasseur, Effect of long term solar variability in a two-dimensional interactive model of the middle atmosphere, *J. Geophys. Res.*, *98*, 20,413–20,427, 1993.

Jackman, C. H., E. L. Fleming, S. Chandra, D. B. Considine, and J. E. Rosenfield, Past, present, and future modeled ozone trends with comparisons to observed trends, *J. Geophys. Res.*, *101*, 28,753–28,767, 1996.

Kuruz, R., The solar spectrum, in *Solar Interior and Atmosphere*, edited by A. N. Cox, W. C. Livingston, and M. S. Matthews, pp. 663–669, Univ. of Ariz. Press, Tucson, 1992.

Kyle, H. L., D. V. Hoyt, J. R. Hickey, R. H. Maschhoff, and B. J. Vallette, Nimbus-7 Earth Radiation Budget calibration history, I, The solar channels, *NASA Ref. Publ.*, *1316*, 1993.

Labitzke, K., and H. vanLoon, Some recent studies of probable connections between solar and atmospheric variability, *Ann. Geophys.*, *11*, 1084–1094, 1993a.

Labitzke, K., and H. vanLoon, Aspects of a decadal Sun-atmosphere connection, in *The Solar Engine and Its Influence on Terrestrial Atmosphere and Climate*, edited by E. Nesme-Ribes, *NATO ASI Ser.*, *Ser. I*, *25*, 381–393, 1993b.

Lacis, A. A., D. J. Wuebbles, and J. A. Logan, Radiative forcing of climate by changes in the vertical distribution of ozone, *J. Geophys. Res.*, *95*, 9971–9981, 1990.

Lawrence, J. K., G. A. Chapman, and S. R. Walton, Weak magnetic fields and solar irradiance variations, *Astrophys. J.*, *375*, 771–774, 1991.

Lean, J., Solar ultraviolet irradiance variations: A review, *J. Geophys. Res.*, *92*, 839–868, 1987.

Lean, J., Contribution of ultraviolet irradiance variations to changes in the Sun's total irradiance, *Science*, *244*, 197–200, 1989.

Lean, J., Variations in the Sun's radiative output, *Rev. Geophys.*, *29*, 505–535, 1991.

Lean, J. L., and D. H. Rind, Climate forcing by changing solar radiation, *J. Clim.*, in press, 1997.

Lean, J., M. VanHoosier, G. Brueckner, D. Prinz, L. Floyd, and K. Edlow, SUSIM/UARS observations of the 120 to 300 nm flux variations during the maximum of the solar cycle: Inferences for the 11-year cycle, *Geophys. Res. Lett.*, *19*, 2203–2206, 1992.

Lean, J., J. Beer, and R. Bradley, Reconstruction of solar irradiance since 1610: Implications for climate change, *Geophys. Res. Lett.*, *22*, 3195–3198, 1995a.

Lean, J. L., O. R. White, and A. Skumanich, On the solar ultraviolet spectral irradiance during the Maunder minimum, *Global Biogeochemical Cycles*, *9*, 171–182, 1995b.

Lee, R. B., III, M. A. Gibson, R. S. Wilson, and S. Thomas, Long-term total solar irradiance variability during sunspot cycle 22, *J. Geophys. Res.*, *100*, 1667–1675, 1995.

Livingston, W. C., L. Wallace, and O. R. White, Spectrum line intensity as a surrogate for solar irradiance variations, *Science*, *240*, 1765–1767, 1988.

London, J., G. J. Rottman, T. N. Woods, and F. Wu, Time variations of solar UV irradiance as measured by the SOLSTICE (UARS) instrument, *Geophys. Res. Lett.*, *20*, 1315–1318, 1993.

McCormack, J. P., and L. L. Hood, Apparent solar cycle variations of upper stratospheric ozone and temperature: Latitude and seasonal dependences, *J. Geophys. Res.*, *101*, 20,933–20,944, 1996.

National Research Council, *Solar Influences on Global Change*, Natl. Acad. Press, Washington, D. C., 1994.

Nishikawa, J., Estimation of total irradiance variations with the CCD solar surface photometer, *Astrophys. J.*, *359*, 235–245, 1991.

Pollack, J. B., W. J. Borucki, and O. B. Toon, Are solar spectral variations a driver for climatic change, *Nature*, *282*, 600–603, 1979.

Predmore, R. E., H. Jacobowitz, and J. R. Hickey, Exospheric cleaning of the Earth Radiation Budget solar radiometer during solar maximum, *Proc. SPIE*, *338*, pp. 104–113, 1982.

Rind, D., and N. K. Balachandran, Modeling the effects of UV variability and the QBO on the troposphere/stratosphere system, II, The troposphere, *J. Clim.*, *8*, 2080–2095, 1995.

Rottman, G. J., Observations of solar UV and EUV variability, *Adv. Space Res.*, *8*(7), 53–66, 1988.

Rottman, G. J., Ultraviolet contribution to the variation of total solar irradiance (abstract), *Eos Trans. AGU*, *76*(46), *Fall Meet. Suppl.*, F93, 1995.

Rottman, G. J., T. N. Woods, and T. P. Sparn, Solar-Stellar Irradiance Comparison Experiment, 1, Instrument design and operation, *J. Geophys. Res.*, *98*, 10,667–10,677, 1993.

Schlesinger, B. M., and R. P. Cebula, Solar variation 1979–1987 estimated from an empirical model for changes with time in the sensitivity of the Solar Backscatter Ultraviolet instrument, *J. Geophys. Res.*, *97*, 10,119–10,134, 1992.

Schlesinger, B. M., and D. F. Heath, A comparison of solar irradiances measured by SBUV, SME and rockets, *J. Geophys. Res.*, *93*, 7091–7103, 1988.

Steinegger, M., P. N. Brandt, and H. F. Haupt, Sunspot irradiance deficit, facular excess, and the energy balance of solar active regions, *Astron. Astrophys.*, *310*, 635–645, 1996.

Thuillier, G., M. Hersé, P. C. Simon, D. Labs, H. Mandel, and D. Gillotay, Observations of the UV solar spectral irradiance between 200 and 350 nm during the Atlas I mission by the solar spectrometer, *Sol. Phys.*, *171*, 283–302, 1997.

Ulrich, R. K., and L. Bertello, Solar-cycle dependence of the Sun's apparent radius in the neutral iron spectral line at 525 nm, *Nature*, *377*, 214–215, 1995.

Vernazza, J. E., E. H. Avrett, and R. Loeser, Structure of the solar chromosphere, II, The underlying photosphere and temperature-minimum region, *Astrophys. J. Suppl. Ser.*, *30*, 1–60, 1976.

Vrsnak, B., D. Placko, and V. Ruzdjak, Calcium plage intensity and solar irradiance variations, *Sol. Phys.*, *133*, 205–213, 1991.

Weber, M., J. P. Burrows, and R. P. Cebula, GOME solar UV/VIS irradiance measurements in 1995 and 1996—First results on proxy activity studies, *Sol. Phys.*, in press, 1997.

White, O. R., and W. C. Livingston, Solar luminosity variation, III, Calcium *K* variation from solar minimum to solar maximum in cycle 21, *Astrophys. J.*, *249*, 798–816, 1981.

White, O. R., G. J. Rottman, and W. C. Livingston, Estimation of the solar Lyman alpha flux from ground based measurements of the Ca II K line, *Geophys. Res. Lett.*, *17*, 575–578, 1990.

Willson, R. C., and H. S. Hudson, A solar cycle of measured and modeled total irradiance, *Nature*, *351*, 42–44, 1991.

Woods, T. N., and G. J. Rottman, Solar Lyman α irradiance measurements during two solar cycles, *J. Geophys. Res.*, *102*, 8769–8779, 1997.

Woods, T. N., G. J. Rottman, and G. Ucker, Solar-Stellar Irradiance Comparison Experiment, 2, Instrument calibration, *J. Geophys. Res.*, *98*, 10,679–10,694, 1993.

Woods, T. N., et al., Validation of the UARS solar ultraviolet irradiances: Comparison with the ATLAS 1 and 2 measurements, *J. Geophys. Res.*, *101*, 9541–9569, 1996.

Wuebbles, D., J. Douglas, E. Kinnison, K. E. Grant, and J. Lean, The effect of solar flux variations and trace gas emissions on recent trends in stratospheric ozone and temperature, *J. Geomagn. Geoelectr.*, *43*, suppl., 709–718, 1991.

J. R. Hickey, Eppley Laboratory, Inc., Newport, RI 02840.

H. L. Kyle, NASA Goddard Space Flight Center, Greenbelt, MD 20771.

J. L. Lean, E. O. Hulburt Center for Space Research, Code 7673L, Naval Research Laboratory, 4555 Overlook Avenue, S.W., Washington, DC 20375-5320. (e-mail: lean@demeter.nrl.navy.mil)

L. C. Puga, NOAA Space Environment Laboratory, Boulder, Colorado.

G. J. Rottman and T. N. Woods, Laboratory for Atmospheric and Space Physics, University of Colorado, Boulder, CO 80303.

(Received December 2, 1996; revised July 18, 1997;
accepted July 22, 1997.)